THE JOURNAL OF PHYSICAL CHEMISTRY B
A JOURNAL OF THE AMERICAN CHEMICAL SOCIETY

pubs.acs.org/JPCB

Article

Liquid Structure and Hydrogen Bonding in Aqueous Hydroxylammonium Nitrate

Daniel D. Depew, Ghanshyam L. Vaghjiani,* Shehan M. Parmar, and Joseph J. Wang

Cite This: *J. Phys. Chem. B* 2024, 128, 824−840

Read Online

ACCESS | Metrics & More | Article Recommendations | Supporting Information

ABSTRACT: Hydroxylammonium nitrate (HAN) has emerged as a promising component in ionic liquid-based spacecraft propellants. However, the physicochemical and structural properties of aqueous HAN have been largely overlooked. The purpose of this study is to investigate the hydrogen bonding in aqueous HAN and understand its implications on these properties and the proton transfer mechanism as a function of concentration. Classical polarizable molecular dynamics simulations have been employed with the APPLE&P force field to analyze the geometry of individual hydrogen bonds and the overall hydrogen-bonding network in various concentrations of aqueous HAN. Radial distribution functions (RDFs) and spatial distribution functions (SDFs) indicate the structural arrangement of the species and their hydrogen bonds. Projections of water density and the orientation of its electric dipole moment near the ions provide insight into the hydrogen-bonding network. The incorporation of water into the hydrogen-bonding network at high ion concentrations occurs via interstitial accommodation around the ions immediately outside the first solvation shell. While ion pairs are observed at all concentrations considered, the frequency of $H_a\cdots O_n$ hydrogen bonds increases substantially with the ion concentration. The findings contribute to a better fundamental understanding of HAN and the precursors of reactivity, crucial to the development of "green" spacecraft propellants.

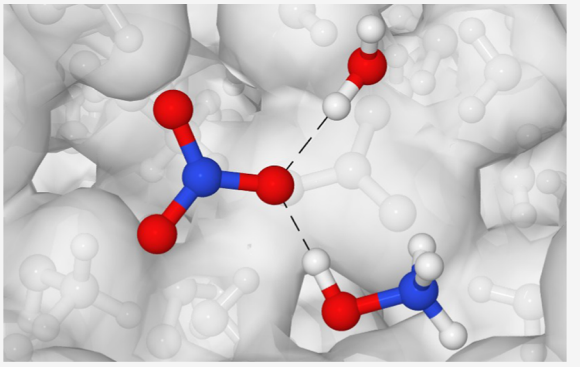

INTRODUCTION

Recently, hydroxylammonium nitrate ($NH_3OH^+ \cdot NO_3^-$, or HAN) has garnered substantial attention for application in a new class of "green" spacecraft propellants.[1,2] In attempting to replace traditional propellants such as hydrazine, HAN-based propellants have been shown to exhibit desirable properties including high energy density, low vapor toxicity, and high chemical and thermal stability.[2−4] Neat HAN exists as an unstable, hygroscopic solid at room temperature with a melting point of 44−48 °C,[5,6] and thus qualifies as an ionic liquid (IL), which is generally defined as a salt with a melting point below 100 °C.[7,8] Because HAN is highly soluble in water and miscible at all concentrations up to the anhydrous salt, it is typically stored in aqueous solution.[9−11]

The decomposition of HAN has been extensively studied due to its initial exploration as a component in liquid gun propellant formulations and subsequent consideration for spacecraft propellant applications.[10−20] Despite this focus on decomposition, many physicochemical and structural properties of aqueous HAN remain inadequately characterized. In the context of liquid gun propellants, early investigations typically concentrated on the overall mixture of HAN with other components, such as triethanolammonium nitrate (TEAN) and water, rather than studying neat or aqueous HAN in isolation. Analogous gaps persist in the literature concerning more recent formulations of spacecraft propellants. The introduction of additional ionic liquids or molecular solvents can result in physical and chemical properties that are challenging to predict, as even binary mixtures may exhibit intricate, nonideal behavior.[21,22] The nuances of the underlying hydrogen-bonding network and structure in neat ionic liquids, as well as in their mixtures, play a crucial role in determining these properties.[23,24]

As it is formed via proton transfer from a Brønsted acid (HNO_3) to a Brønsted base (NH_2OH), HAN may be further characterized as a protic ionic liquid (PIL). Extensive work has been done on PILs over the past 20 years and the field continues to grow—see comprehensive reviews by Greaves and Drummond.[7,25] However, HAN is almost never included in surveys of PILs. The scarcity of existing experimental data may be one reason, but the high energy density of anhydrous HAN, along with the elevated temperature and instability associated with its melted state, likely deters comparative studies due to potential safety concerns. Additionally, HAN is not used in

Received: August 20, 2023
Revised: December 4, 2023
Accepted: December 18, 2023
Published: January 9, 2024

organic synthesis, a primary application of PILs and ILs more broadly, which may contribute to its exclusion from such studies. For comparison with HAN, the most relevant PILs are the primary alkylammonium nitrates: methylammonium nitrate (MAN), ethylammonium nitrate (EAN), propylammonium nitrate (PAN), and butylammonium nitrate (BAN). Numerous studies have been conducted on the effect of alkyl chain length on the physicochemical and structural properties of these liquids, both neat and mixed with water.[26−35] Generally, increasing the alkyl chain length results in a decreased density and increased dynamic viscosity. Nanostructure exhibiting intermediate range order is observed for these nitrates containing a chain length of at least two (i.e., EAN or larger), but it was not observed for MAN. The longer alkyl chains introduce a separation of polar and apolar domains on the cations, enabling these PILs to promote amphiphilic self-assembly. Interestingly, their nanostructure is retained with the addition of water, although the viscosities decrease.

HAN should display far more similarity to MAN than longer-chain alkylammonium nitrates, and thus, care must be taken when drawing comparisons to these liquids. Indeed, HAN differs from MAN only in the substitution of the methyl group for a hydroxyl, so short-range ordering as found in MAN seems likely. The hydroxyl groups set HAN apart from most other ammonium-based nitrates. All such PILs can be expected to form relatively strong protic N−H···O hydrogen bonds; however, the alkylammonium nitrates may contribute weak aprotic C−H···O H-bonds along the alkyl chains,[36] whereas the O−H···O from the hydroxylammonium cation should be significantly stronger. The role of the hydroxyl in PILs was investigated by comparing EAN with ethanolammonium nitrate (EtAN), and it was concluded that the hydroxyl acts as a kind of "solvophobic switch" that decreases correlation length and leads to small clusters of ions in the bulk instead of the extended network observed in EAN.[31]

The existence of hydrogen bonding in PILs was first definitively proven for EAN in 2009, with the detected three-dimensional H-bond networks described as structurally reminiscent of water.[26] A variety of hydrogen bonds have been found in PILs, from strong linear H-bonds to weaker bent ones.[23] The nature of these H-bonds has been correlated to multiple properties of PILs, including melting point, ionic conductivity, viscosity, and ionicity.[23,34] On the other hand, previous studies have cautioned against overemphasizing the importance of hydrogen bonding in determining the structure of ILs,[24,37] noting that 3D H-bond networks are confined within the polar domain of the liquid's nanostructure. Such caution is unwarranted for the HAN system as it is predominantly polar, lacking apolar domains that would allow for segregation. Further, mixtures of PILs with water have been contextualized based on hydrogen bonding, with the degree of H-bond network disruption by the solvent governing their interactions.[25]

Considering the above, a careful study of hydrogen bonding in aqueous HAN should lead to a better fundamental understanding of HAN in propellants. While hydrogen bonding has been shown in the HAN crystal structure[38] and long-predicted in the condensed phase,[5,9,14,39] to date there have been no atomistic studies of the structure of aqueous HAN. In this work, classical molecular dynamics (MD) simulations are performed to investigate hydrogen bonding in various concentrations of aqueous HAN. For H-bonds in the classical MD simulations which impose fixed intramolecular connectivity, "donor" refers unambiguously to the atom which is covalently bonded to the hydrogen atom. The geometry of individual H-bonds is considered in conjunction with the overall H-bonding network. Special attention is directed toward understanding how water is incorporated into the network and its impact on physicochemical properties. Throughout the article, implications of structural changes on HAN reactivity and proton transfer are discussed as the system becomes more concentrated.

COMPUTATIONAL METHODS

The fully atomistic, polarizable APPLE&P force field was used for the MD simulations in this work. Expanding on the original APPLE&P force field,[40] revised parameters were used for the NO_3^- anion,[41] and a new force field description for the NH_3OH^+ cation was developed following the standard procedure described previously.[40] Water was treated using the SWM4-DP model.[42] Figure 1 depicts these species and indicates the atom labeling scheme used in this work.

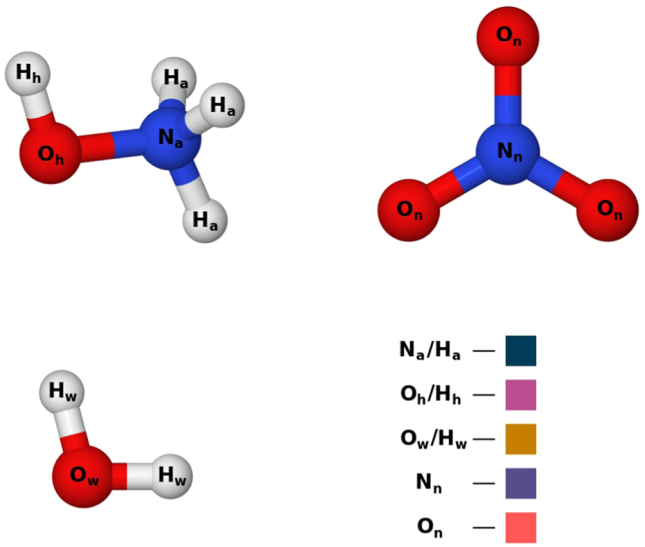

Figure 1. Labels for different atom types in the aqueous HAN system. Subscripts describe either the functional group in the cation (i.e., hydroxyl or ammonium) or molecule type (i.e., nitrate or water). At the bottom right, a color key is presented, which represents the atom types in all subsequent figures and plots.

MD simulations of bulk aqueous HAN were conducted at 298 K using the WMI-MD package, which was recently extended to handle long-range charge/induced dipole and induced dipole/induced dipole interactions. The Ewald summation method was used for the treatment of all long-range electrostatic forces between the partial atomic charges and aforementioned induced dipole interactions. Induced dipoles were computed via direct iteration with a predictor-corrector method. A cutoff radius of 13 Å was used for all van der Waals interactions and the real part of electrostatic interactions in the Ewald summation. Thole screening (a_T = 0.2) was utilized to dampen induced dipole/induced dipole interactions within 6 Å in order to avoid the polarization catastrophe.[43] Covalent bond lengths were constrained using the velocity-Verlet form of the SHAKE algorithm.[44] A multiple-time-step reversible reference system propagator algorithm was employed for efficiency in the integration of interactions occurring on different time scales.[45] The time steps implemented were: 0.25 fs for bonds, bends, and out-of-plane motions; 1.5 fs for torsions and nonbonded

https://doi.org/10.1021/acs.jpcb.3c05623
J. Phys. Chem. B 2024, 128, 824−840

interactions within 7 Å; and 3.0 fs for all other nonbonded interactions.

To investigate the effect of the concentration, four systems with varying ion mole fractions were assembled in periodic cubic simulation boxes. The concentrations were primarily chosen for validation of the force field with experimental density values from ref 46. Initially, each system was configured in the gas phase by randomly positioning molecules in a simulation box that measured 50 Å per side. A brief MD simulation was then performed to shrink the cell isokinetically to the experimental density. Subsequently, each system was equilibrated in the isothermal−isobaric (NPT) ensemble at 298 K for 3−5 ns before additional NPT runs of 48 ns were performed to compute densities. Details of the system compositions with equilibrium cell sizes are presented in Table 1. These cell sizes were then utilized to perform production runs in the canonical (NVT) ensemble of 45 ns for the two lower HAN concentrations and 102 ns for the two higher concentrations.

Table 1. Composition of Simulated HAN/Water Systems

number of HAN/H_2O	ion mole fraction χ	molarity (mol/L)	cell size (Å)
80/1384	0.0546	2.76	36.37
180/930	0.1622	6.89	35.14
330/440	0.4286	12.72	35.06
432/126	0.7742	16.13	35.43

RESULTS AND DISCUSSION

Bulk Density and Excess Molar Volume. The computed bulk-phase densities for the four HAN concentrations at 298 K are plotted in Figure 2a. These densities are also compared with experimental values from the literature, which were measured at 293 K.[10,46] Error bars for the densities were not reported for the experimental data, but for the MD simulations, the errors due to finite sampling are easily estimated to be on the order of $\delta\rho \approx 10^{-4}$ g cm^{-3} or less, well inside the markers in Figure 2a. Time series plots and Gaussian fits to the density samples can be found in the Supporting Information (Figures S1 and S2). The excess molar volume V_m^E was also calculated for the MD and experimental data using eq 1 and is plotted in Figure 2b.

$$V_m^E = \frac{x_{HAN}M_{HAN} + x_{H_2O}M_{H_2O}}{\rho} - \frac{x_{HAN}M_{HAN}}{\rho_{HAN}} - \frac{x_{H_2O}M_{H_2O}}{\rho_{H_2O}} \quad (1)$$

Here, x_{HAN} and x_{H_2O} are the mole fractions, M_{HAN} and M_{H_2O} are the molar masses, ρ_{HAN} and ρ_{H_2O} are the mass densities of the two components, and ρ is the mass density of the overall mixture.

NPT simulations of neat (anhydrous) HAN did not stabilize to an equilibrium density at 298 K. Instead, these simulations exhibited substantial density fluctuations, suggesting that the system was near a phase transition. Given that the melting point of HAN is around 44−48 °C,[5,6] this behavior is not unexpected. Consequently, when computing all excess molar volumes, a reference density of ρ_{HAN} = 1.68 g cm^{-3} was utilized for neat (anhydrous) HAN,[46] even though the temperature for this measurement was not reported but presumably was above the melting point. A simple error analysis elucidates how the uncertainty in ρ_{HAN} profoundly impacts the calculation of the excess molar volume at higher ion mole fraction χ. As the experimental density for neat HAN was only reported to two decimal points of precision, a lower-bound estimate of the uncertainty in V_m^E can be obtained by assuming that $\delta\rho_{HAN}$ = 0.01 is the dominant source of error. This leads to the error bars shown in Figure 2b.

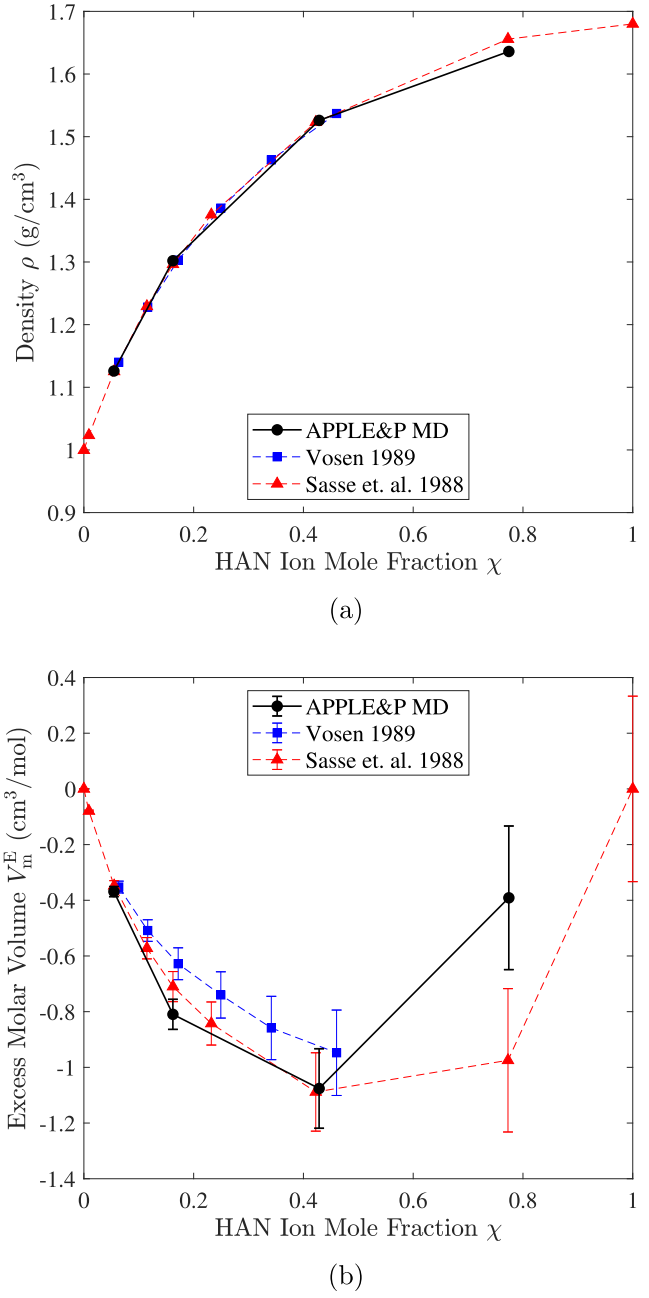

Figure 2. (a) Density and (b) estimated excess molar volume as a function of ion mole fraction in aqueous hydroxylammonium nitrate (HAN). The simulation values were computed at 298 K, and the experimental values were measured at 293 K. As a guide to the eye, solid and dashed lines connect the values for simulation and experiments, respectively. The experimental density for molten HAN[46] was used as the reference for χ = 1.

Bahadur et al.[47] demonstrated that the effect of temperature on V_m^E is minor for other aqueous ammonium ionic liquid mixtures at both low and high mole fractions of IL. Therefore, while the use of a reference ρ_{HAN} taken at a higher temperature

https://doi.org/10.1021/acs.jpcb.3c05623
J. Phys. Chem. B 2024, 128, 824−840

likely contributes to discrepancies in the V_m^E of Figure 2b (particularly at higher ion mole fraction χ), the qualitative behavior should remain the same—specifically, a negative excess molar volume across the range of concentrations considered. Disagreement near $\chi = 0.77$ may also be due to the force field description of ionic interactions. While developing the force field's repulsion-dispersion parameters, it was deemed necessary to trade accuracy in predicting density in order to preserve HAN's miscibility with water. Moreover, it is difficult to assess the reliability of the experimental density measurements, as the sources provided limited information on the experimental methods.

The nonideal mixing behavior indicated by the negative excess molar volume may suggest stronger interactions between the IL and solvent than those in the neat IL or the neat solvent.[25] Similar observations of negative V_m^E were made for ethylammonium nitrate (EAN) and propylammonium nitrate (PAN), where, interestingly, both PILs also displayed positive excess molar enthalpy H_m^E. The latter typically implies a weakening of IL−solvent interaction upon mixing.[33] This seemingly paradoxical outcome was rationalized by hypothesizing an interstitial accommodation in the liquid structure. For HAN, whose cation is comparatively small and polar, ion−dipole attractions, hydrogen bonding, and packing effects all play roles in the observed negative excess molar volume. Further analysis of the structural data, to be addressed in subsequent sections, is required to elucidate these effects.

Radial Distribution Functions. Figure 3 presents the site−site radial distribution functions (RDFs) depicting hydrogen-bonding interactions at the ion concentration $\chi = 0.43$. Within the three unique oxygen species in the system, only the oxygen atoms in water (O_w) and nitrate (O_n) serve as legitimate hydrogen bond acceptors. Although the RDFs for hydroxylammonium oxygen (O_h, Figure S3) do show weak interactions, represented by shoulders around 3 Å, these are not included in our subsequent analysis due to their weak nature. This observation aligns with previous simulations of its conjugate base NH_2OH.[48] The locations of the first maximum and minimum for each RDF, which indicate the primary peak positions and the start of the second coordination shell, respectively, are summarized in Table 2. These positions suggest moderately strong hydrogen bonds, with the bond strength increasing as the distance to the first maximum decreases. From Figure 3, it is evident that cation−anion interactions dominate the hydrogen-bonding landscape at this concentration. The cation's hydroxyl and the nitrate oxygen form the strongest hydrogen bond in the system, corroborating conclusions drawn from infrared (IR) studies.[39] Although the NH_3OH^+ hydroxyl also forms a strong bond with the water oxygen, this interaction is marginally weaker, and its peak is less pronounced. Interestingly, the aprotic hydrogen bonds formed by the cation's hydroxyl group (O_h−H_h···O) appear stronger than the protic hydrogen bonds it forms through its ammonium group (N_a−H_a···O), irrespective of the acceptor—NO_3^- or H_2O. This suggests that the cation's hydroxyl group plays a pivotal role in hydrogen bonding within the system. The weakest hydrogen bonds in the system are those between the water molecules themselves. This aligns with the expectations set by prior studies, which hypothesize that the doubly ionic hydrogen bonds in ion−ion interactions and ionic hydrogen bonds in ion−water interactions are generally stronger than the prototypical water−water hydrogen bonds (O_w−H_w···O_w).[36,49]

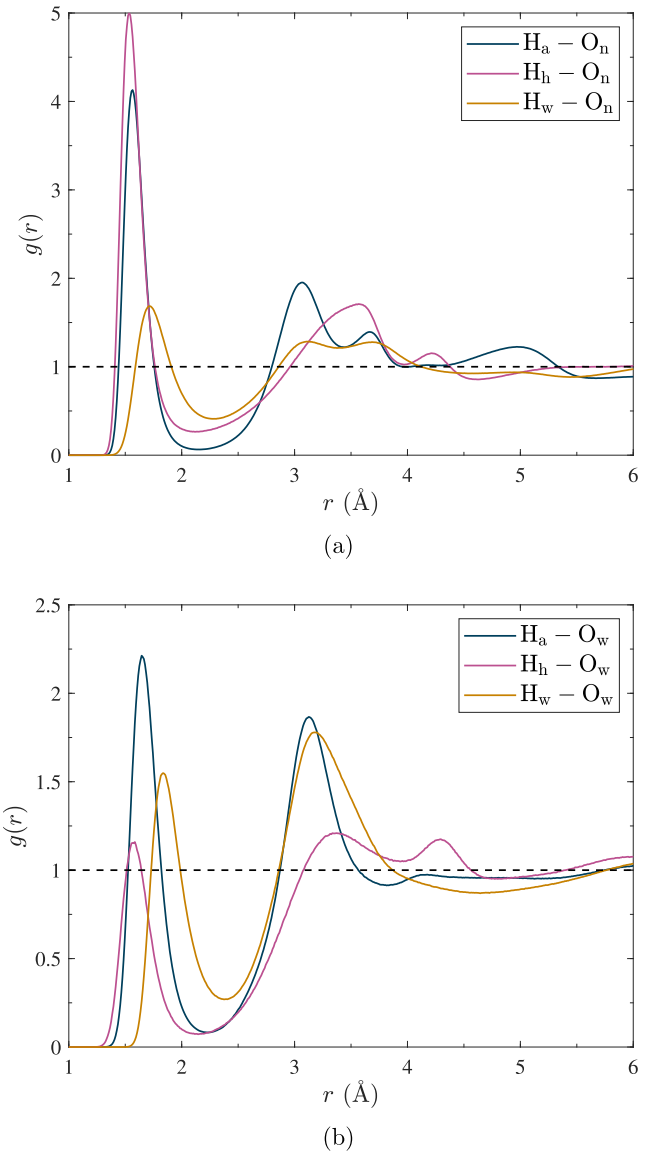

Figure 3. Site−site radial distribution functions in HAN with ion mole fraction $\chi = 0.43$ at 298 K for hydrogens H-bonding with (a) anion oxygen O_n and (b) water oxygen O_w.

Table 2. Distance to the First Maximum and First Minimum of the H-Bond RDFs in HAN at Mole Fraction $\chi = 0.43$

hydrogen bond type	r_{max} (Å)	r_{min} (Å)
H_a···O_n	1.57	2.16
H_h···O_n	1.54	2.14
H_w···O_n	1.72	2.29
H_a···O_w	1.66	2.24
H_h···O_w	1.58	2.14
H_w···O_w	1.84	2.39

In order to assess the influence of concentration on hydrogen bonding and coordination within HAN, "unnormalized" radial distribution functions, denoted as $\hat{\rho}g(r)$, were computed for each hydrogen bond donor−acceptor pair.[50] This functional form is related to the calculation of the coordination number with respect to a target atom species via the spherical integral:

$$N_{coord} = \int_0^R 4\pi r^2 \hat{\rho} g(r)\, dr \quad (2)$$

https://doi.org/10.1021/acs.jpcb.3c05623
J. Phys. Chem. B 2024, 128, 824−840

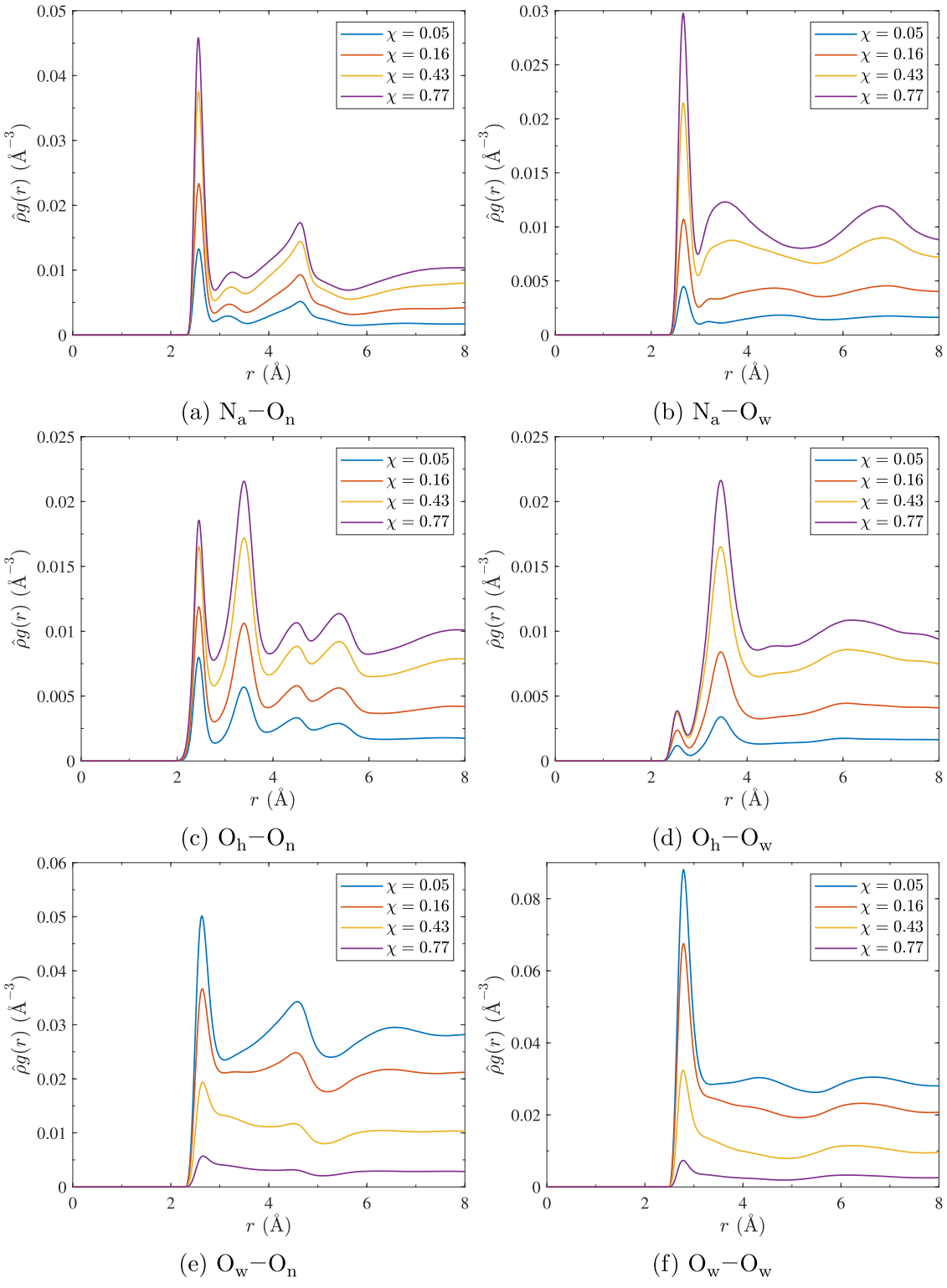

Figure 4. Hydrogen bond donor density distributions for aqueous HAN at varying mole fractions. The RDF $g(r)$ is multiplied by the donor bulk atomic density $\hat{\rho}_{donor}$.

In this equation, r is the distance between donor and acceptor atoms, R is the position of the first minimum in the radial distribution function $g(r)$, and $\hat{\rho}$ is the average number density (in Å^{-3}) of the target atom type in the bulk. This unnormalized form of the RDF makes explicit the concentration dependence, as it represents the local number density of the target atom as a function of distance from the other atom in the pair. The target atom density can be specified using either $\hat{\rho}_{donor}$ or $\hat{\rho}_{acceptor}$; in this analysis, $\hat{\rho}_{donor}$ was employed.

The unnormalized RDFs are plotted in Figure 4. In each case, an increase in ion concentration leads to an increase in coordination with the NH_3OH^+ cation (Figure 4a–d). Regardless of the concentration, cation–anion coordination consistently surpasses cation–water coordination. This is

https://doi.org/10.1021/acs.jpcb.3c05623
J. Phys. Chem. B 2024, 128, 824–840

evidenced by the absolute height of the first maxima when Figure 4a is compared with 4b and 4c is compared with 4d. Water is well-incorporated into the hydrogen-bonding network at all concentrations when considered as a donor species, as the first peaks in the bottom row of Figure 4e,f are of comparable height. A subtle preference for water−water aggregation exists over water−anion aggregation at all concentrations, which has been documented previously for ILs with moderately basic anions including nitrate.[51] The second maxima for the cation's N_a and O_h atoms at just above 3 Å arise from hydrogen bonds formed by the other donor in the cation (i.e., O_h and N_a, respectively). Consequently, comparing Figure 4a,c reveals that growth in anion H-bonding with N_a outpaces H-bonding with O_h as the ion concentration increases. This has practical implications on the proton transfer reaction

$$NH_3OH^+ + NO_3^- \rightarrow NH_2OH + HNO_3$$

as direct proton transfer would be preceded by the formation of a $N_a{-}H_a{\cdots}O_n$ H-bond.

H-Bond Donor−Acceptor Coordination Numbers. The coordination numbers for the pairs of hydrogen bond donors and acceptors are listed in Table 3. The nomenclature adopted here is important: the "donor coordination number" refers to the number of neighboring acceptor atoms that surround a particular donor atom, whereas the "acceptor coordination number" refers to the number of neighboring donor atoms that surround a particular acceptor atom. Thus, in eq 2, $\hat{\rho}_{acceptor}$ was used to compute the donor coordination number, and $\hat{\rho}_{donor}$ was used to compute the acceptor coordination number. The integrals were performed up to the first minimum in each corresponding RDF except where indicated by a footnote. The donor coordination numbers in the upper half of the table highlight the role of the donor atom in determining the liquid structure. Because it is an estimate of the total number of hydrogen bonds formed by a reference donor atom with a particular target acceptor atom type, it scales qualitatively as the number of covalently bonded hydrogens per donor group, assuming all hydrogens are able to form H-bonds. In this system, the NH_3OH^+ cation has 4 hydrogens available for hydrogen bonding (3 per ammonium group through N_a, 1 per hydroxyl group through O_h), while H_2O has only 2 available hydrogens. Accordingly, it is observed that the coordination number of N_a exceeds that of O_h across all concentrations, but the relationship is more complex than a direct correlation to the 3:1 ratio of H_a to H_h hydrogens. For example, the coordination number for the donor O_h atom surpasses one for the $O_h{-}O_n$ interactions at higher concentrations, suggesting that the single hydrogen of the cation's hydroxyl group can form bifurcated hydrogen bonds.

Table 3. Coordination Numbers for H-Bond Donor/Acceptor Atom Pairs in Aqueous HAN at Increasing Ion Mole Fraction

interaction		donor coordination number			
donor/acceptor type	atom−atom	χ = 0.05	χ = 0.16	χ = 0.43	χ = 0.77
cation/anion	$O_h{-}O_n$	0.54	0.82	1.20	1.42
	$N_a{-}O_n$	0.83	1.48	2.30	2.85
cation/water	$O_h{-}O_w$	0.50	0.30	0.12	0.03
	$N_a{-}O_w$	2.11	1.51	0.76	0.23
water/anion	$O_w{-}O_n$	0.37	0.94	2.06[a]	2.83[a]
water/water	$O_w{-}O_w$	3.96	3.31[a]	1.54[a]	0.32[a]
interaction		acceptor coordination number			
donor/acceptor type	atom−atom	χ = 0.05	χ = 0.16	χ = 0.43	χ = 0.77
cation/anion	$O_h{-}O_n$	0.18	0.27	0.40	0.47
	$N_a{-}O_n$	0.28	0.49	0.77	0.95
cation/water	$O_h{-}O_w$	0.03	0.06	0.09	0.09
	$N_a{-}O_w$	0.12	0.29	0.57	0.78
water/anion	$O_w{-}O_n$	2.11	1.61	0.92[a]	0.27[a]
water/water	$O_w{-}O_w$	3.96	3.31[a]	1.54[a]	0.32[a]

[a]Integral truncated at the inflection point in $g(r)$ corresponding to a shoulder feature after the first maximum but prior to the first minimum.

The acceptor coordination numbers are given in the lower half of Table 3. Conversely to the donor coordination numbers, these values approximate the number of hydrogen bonds a reference acceptor atom forms with a particular target donor atom type. As the total number of hydrogen atoms increases for a specific donor type, the likelihood of forming a hydrogen bond increases as well. Notably, water oxygen displays very low coordination with the cation's hydroxyl group across all concentrations, despite $O_h{-}H_h{\cdots}O_w$ having the shortest hydrogen bond length of any $X{-}H{\cdots}O_w$ interaction (see Figure 3b and Table 2). This further underscores the complexity of hydrogen bonding within the liquid structure.

When acting as a hydrogen bond donor, the coordination numbers for water O_w exhibit a peculiar behavior in Table 3. First, as computed with eq 2, the coordination numbers cannot distinguish between the roles of the donor and acceptor for homonuclear $O_w{-}O_w$ hydrogen bonds. Moreover, the noted outliers in the last two rows of the table stem from the presence of shoulders in the radial distribution functions of the $O_w{-}O_n$ and $O_w{-}O_w$ at higher concentrations. An in-depth discussion regarding the origins of these shoulders will follow in a subsequent section.

Although the donor−acceptor coordination numbers detailed in Table 3 provide valuable insight, there is some inherent ambiguity in interpreting them. The homonuclear $O_w{-}O_w$ interaction offers one such example. Additionally, when assessing the coordination number for a hydrogen bond donor, neither the precise configuration nor the angle of the hydrogen bonds are considered. Consequently, one donor−acceptor pair might appear to be more coordinated than another pair simply because the bonds formed by the former pair are oriented in a way that fits more neatly into the spherical boundary used to compute the coordination number. This ambiguity can be partially mitigated by instead analyzing the H···O hydrogen bonds directly since the first minima in the hydrogen bond RDFs are clearly defined for all interactions.

Sankey diagrams are helpful tools to visualize changes in the hydrogen-bonding topology as the ion concentration is varied. Diagrams were created for the HAN system at each concentration using the TRAVIS software.[52,53] In Figure 5, each node on the left corresponds to a particular hydrogen atom type (i.e., H_h, H_a, or H_w), and each node on the right corresponds to an acceptor atom type (i.e., O_n or O_w). To enhance visual clarity, node widths are normalized on a per-atom basis, meaning the absolute width of a node is scaled to the number of hydrogen bonds formed per hydrogen type or acceptor type. This normalization results in a nontraditional link representation where the link width varies between nodes, but it enables simple side-by-side comparison across concentrations. [Footnote: The node width scaling is related to the sums in the coordination number columns from Table 3. The left node

https://doi.org/10.1021/acs.jpcb.3c05623
J. Phys. Chem. B 2024, 128, 824−840

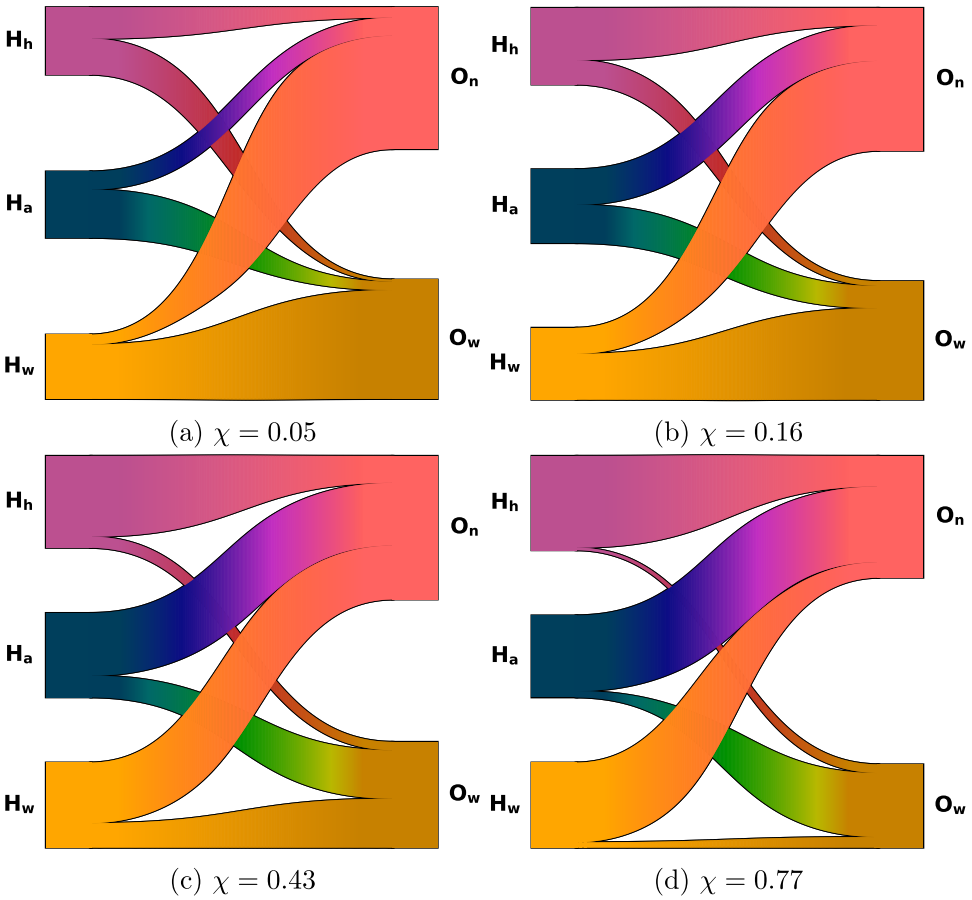

Figure 5. Hydrogen-bonding topology in aqueous HAN at varying ion mole fractions with donors on the left and acceptors on the right. The width of each connection is scaled according to the number of hydrogen bonds between each donor/acceptor pair.

widths are scaled approximately to the sum of the *donor* coordination numbers (divided by the hydrogen count per donor) and the right node widths are scaled approximately to the sum of the *acceptor* coordination numbers. However, the coordination numbers for homonuclear O_w−O_w distort this approximation.]

Consider the relative link widths at the oxygen (acceptor) nodes in each diagram. At the lowest concentration (Figure 5a), water molecules significantly outnumber the ions, and the majority of the anion's hydrogen bonds originate from O_w−H_w···O_n linkages. The same is true for the hydrogen bonds involving the water oxygen O_w, which primarily originate from O_w−H_w···O_w coordination with other water molecules. However, at the highest ion concentration (Figure 5d), the substantial increase in the population of H_h and H_a atoms inversely affects the availability of water molecules to form hydrogen bonds with either O_n or O_w.

Moreover, the evolving link widths illustrate the enhancement of ion pairs and aggregate formation as the ion concentration is increased. These results align with previous IR studies of aqueous HAN, which noted a reduction in nitrate hydration and the emergence of ion pairs as the dominant species at ion concentrations beyond 8 M (χ = 0.20).[39] The authors observed a splitting of the $\nu_3(NO_3^-)$ mode, attributing the band near 1300 cm^{-1} to ion-paired nitrate. This band shifts linearly toward lower frequency for increasing ion concentrations from 0.8 to 16 M. However, the linear behavior is disrupted at concentrations below 0.8 M (χ = 0.014), leading the authors to suggest this concentration as the onset of significant ion pairing. Notably, the MD simulation performed in this work at an ion mole fraction of χ = 0.05 indicates that 80% of the cations form at least one hydrogen bond with an anion.

The diagrams in Figure 5b also illustrate the strength and stability of the interionic O_h−H_h···O_n hydrogen bond between the cation's hydroxyl group and the nitrate oxygen. For instance, the outgoing link from H_h to O_n comprises over two-thirds of the hydrogen bonds formed by the hydroxyl, while O_n accounts for only 36.7% of acceptor atoms in the system. At the highest concentration in Figure 5d, this link width grows to 97.3% of the hydroxyl hydrogen bonds, whereas 91.1% of acceptors in the system are O_n atoms. Oxygen is generally recognized as a more efficient hydrogen bond donor than nitrogen,[36] but in the HAN system, the N_a atom acts as the cationic center and its protic N_a−H_a moiety outnumbers the aprotic O_h−H_h by a factor of 3. A result of these combined effects is that the rate of ammonium−nitrate coordination surpasses that of hydroxyl−nitrate coordination with increasing ion concentration. At lower ion concentrations, the competitive hydrogen-bonding environment favors the better donor species (i.e., O_h), but as water is removed from the system, more nitrate oxygen (O_n) becomes available for hydrogen bonding with the ammonium group.

The system with an ion mole fraction of χ = 0.43 warrants additional attention, as it most closely approximates equimolar conditions among those simulated. Within this system, the nearly equal distribution of the anion's hydrogen bonds among donor species suggests that the water is well incorporated into the IL's hydrogen-bonding network. Additionally, inspection of the H_a node in Figure 5c indicates that the cation's ammonium

https://doi.org/10.1021/acs.jpcb.3c05623
J. Phys. Chem. B 2024, 128, 824−840

group continues to donate around a quarter of its $N_a-H_a\cdots O$ hydrogen bonds to water molecules in these conditions. With the intrinsic strength of the $O_h-H_h\cdots O_n$ hydrogen bond, the moderate-strength $N_a-H_a\cdots O_w$ hydrogen bond plays a critical role in ensuring the miscibility of the ionic liquid with water.

Spatial Distribution Functions. The three-dimensional solvation structure around the water and ions is more easily unraveled by working with spatial distribution functions (SDFs). Figure 6 shows selected isosurfaces normalized by the average atomic density of each species for the χ = 0.43 simulation. Isosurface colors for the solvating atoms are consistent with the colors for the atom types from Figure 1. For the water molecule in Figure 6a, only isosurfaces for distances up to the first minimum of the corresponding O···H RDFs are included, and all isosurfaces are displayed at a contour level of $4\hat{\rho}_{target}$ for each observed target atom type. The solid surfaces represent acceptors H-bonding with the water, whereas the meshed surfaces represent the hydrogen types covalently bonded to the H-bond donors. It may be helpful to reference Figure 5c while viewing this SDF. Solid surfaces correspond to the outgoing connections from the water H_w on the bottom left of the diagram. Stronger and more plentiful hydrogen bonds are formed with the anions than with other water molecules at this concentration. Mesh surfaces in the SDF correspond to the incoming connections to water O_w on the bottom right of Figure 5c, matched by color. Most of the fuchsia H_h surface is inside the blue H_a surface, which itself is primarily within the gold H_w surface. The tetrahedral geometry displayed by these surfaces is characteristic of the TIP4P water model, closely related to the SWM4-DP model used in this work.[54,55] Orientation of the salmon O_n is similar to the SDFs presented in a Car−Parrinello molecular dynamics (CPMD) simulation of 1.6 wt % monomethylammonium nitrate (MAN) by Zahn et al.,[29] indicative of linear hydrogen bonding. In that study, however, the tetrahedral configuration of the ammonium donors was more pronounced, with none of the H_a isosurfaces lying in the molecular plane of the water.

The various hydrogen types around the nitrate anion are again shown as mesh surfaces in Figure 6b. Water oxygen is depicted as the solid surface, and all isosurfaces are at a contour level of $4\hat{\rho}_{target}$. As with the water SDF, only surfaces contained within the first minimum of the corresponding RDF are included. The overlapping H_h and H_a surfaces from the cation show a weak preference for coordination along the anion's N−O bond. Meanwhile, H_w coordinates off-axis in an orientation more aligned with the anion's HOMO lone pairs of the sp^2 oxygens. This geometry for O_n-H_w hydrogen bonds is consistent with previous *ab initio* MD and QM/MM studies.[56,57] Because each O_n contains two lone pairs on average, this geometry suggests that it may function as a bifurcated acceptor and accept two hydrogen bonds simultaneously. No chelation is observed with respect to a single water molecule, however, as the O_w surface is offset behind the hydrogen at nearly exactly the intramolecular O_w-H_w bond distance (0.97 Å) to form a monodentate linear H-bond. At this concentration and contour level, the H_w surface forms a nearly complete spherical ring. The development of the upper and lower portions of this ring is diminished and the ring's width grows as ion concentration increases. This effect may be rationalized by two explanations. First, at low ion concentration, the abundance of water molecules must compete with one another for the preferred off-axis coordination with O_n, leading to more hydrogen bonds formed above and below the anion plane and enhancing the upper/lower ring structure.[58] As the ion concentration increases, however, the stronger and generally on-axis cation−anion hydrogen bonds relegate the water to coordinate further off-axis. No H_w is observed inside the upper and lower O_w lobes along the nitrate C_3 axis, so these regions do not constitute hydrogen bonding to the nitrate and instead suggest that the anion is solvated in different conical shells.[57]

It is somewhat surprising that the cation's hydrogens do not exhibit a similar geometry around the nitrate as the water. Previous DFT studies of HAN which employed an implicit

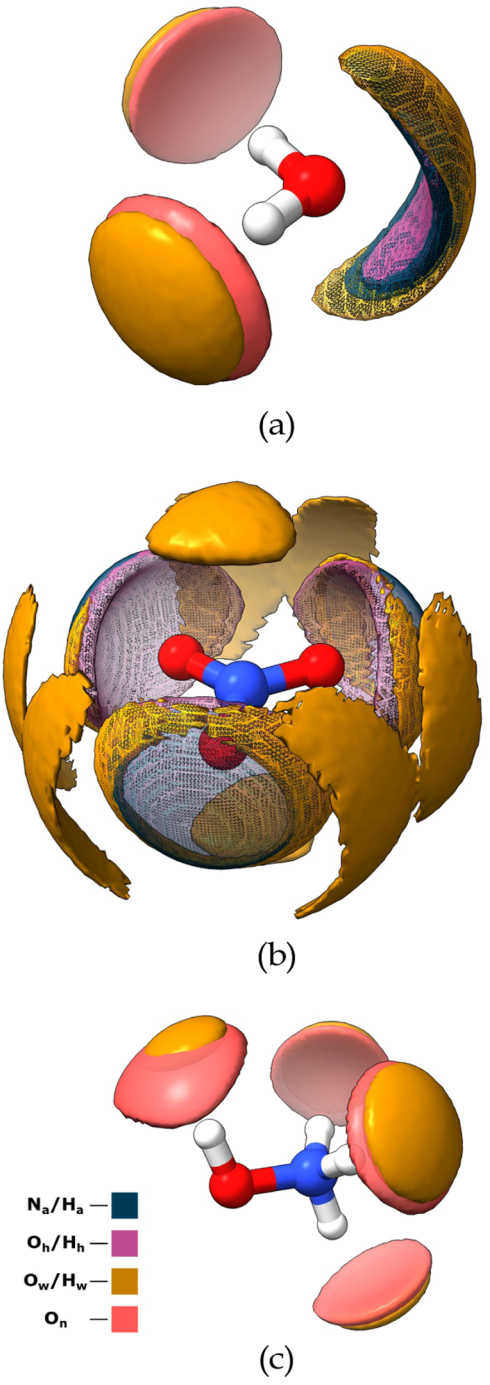

Figure 6. Spatial distribution functions in HAN at ion mole fraction χ = 0.43 around (a) water, (b) anion, and (c) cation. Surfaces are colored by target atom using the same color scheme as in Figure 1. A key is provided in (c) for clarity. Meshed surfaces indicate hydrogen, while continuous surfaces represent heavy atoms. The isosurface contour level is $4\hat{\rho}_{target}$ in each SDF.

https://doi.org/10.1021/acs.jpcb.3c05623
J. Phys. Chem. B 2024, 128, 824−840

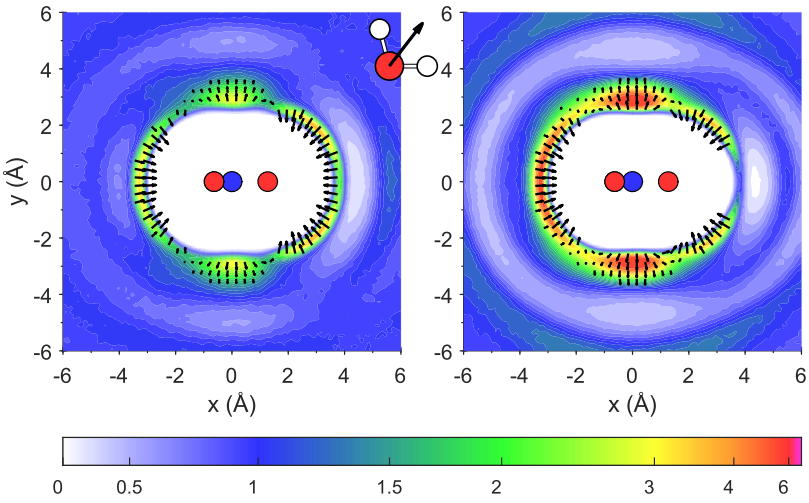

Figure 7. Projection of water oxygen density into the plane orthogonal to the nitrate anion in HAN at ion mole fractions of $\chi = 0.05$ (left) and 0.77 (right). One N−O bond is placed on the $+x$-axis and the projection samples a width of 1 Å on either side of the plane. Arrows indicate the average direction of the water dipole moment vector, as defined in the schematic (not to scale). The arrows are included in regions where $\hat{\rho}_{O_w} \geq 1.5$. Larger arrows indicate a higher likelihood of orientation.

solvent model reported optimized ion pair geometries with noticeably nonlinear $N_n{-}O_n{\cdots}H_a$ and $N_n{-}O_n{\cdots}H_h$ angles,[20,59] though such isolated calculations cannot be reliably used to infer the bulk H-bonding structure of the explicit cosolvents. Perhaps more tellingly, a CPMD simulation of neat MAN generated SDFs where the H_a hydrogens strongly preferred an off-axis coordination with the nitrate N−O bond.[28] In fact, even at a low contour level, none of the H_a isosurface was aligned with this bond. Similar behavior was observed in classical MD simulations of other primary alkylammonium nitrate ILs (EAN, PAN, and BAN).[60] It remains unclear whether the H_h and H_a surfaces in Figure 6b represent the true structure in HAN or whether it is a limitation of the force field used in this work.

Before proceeding, it is important to emphasize how SDFs are typically constructed. Specifically, a *reference frame* must be selected for the reference molecule which specifies an origin and unambiguous orientation of the reference coordinate axes. Often (and indeed in this work), three atoms are chosen such that the first atom is placed at the origin, the second defines a fixed direction (e.g., along the $+x$-axis), and the third defines a plane containing all three atoms. For nonrigid molecules, the absolute positions of the reference molecule's atoms are not constant, leading to a "smearing" effect in the SDF as different molecular conformations are sampled. Thus, the choice of reference frame is a vital yet rarely discussed aspect when analyzing structure via SDF. The NH_3OH^+ cation contains a very low torsional barrier about the N−O bond, calculated to be <1.1 kcal/mol via gas-phase DFT as part of the force field parametrization in this work. At this barrier height, the hydroxyl is nearly a free rotor, but the staggered conformation is statistically most likely as steric hindrance is minimized between the hydroxyl and ammonium groups. In order to obtain a local picture of the cation's hydrogen-bonding interactions then, any suitable SDF must be split into two regions by functional group.

Figure 6c depicts the position of the two H-bond acceptor species, O_n (salmon) and O_w (orange) around the cation using the regions just described. The hydroxyl region places O_h at the origin, N_a along the $+x$-axis, and H_h in the xy-plane. The ammonium region uses a reference frame with N_a at the origin, O_h along the $-x$-axis, and an arbitrary H_a in the xy-plane. In this way, both the cation σ mirror plane and the N−O bond are aligned in both reference frames. To create the figure, coordinates for the ammonium region of the SDF were translated by the N−O bond length so that the reference molecules were aligned for both regions. Then, as in Figure 6a,b, only isosurfaces at distances within the first minimum of the RDF are shown, again with a contour level of $4\hat{\rho}_{target}$. It is clear from Figures 3b and 5c that not many $O_h{-}H_h{\cdots}O_w$ hydrogen bonds are formed at this concentration, yet those that do exist contain a notably linear H-bond angle. In contrast, the stronger $O_h{-}H_h{\cdots}O_n$ hydrogen bonds display more nonlinear coordination. This nonlinearity disappears at very high contour levels, however, indicating that a H-bond angle of 180° is still the *most likely* geometry.

The leftward bias of the salmon O_n surface in this region may be due to several distinct factors. First, there is a degree of anharmonicity present in the cation's H−O−N bend, with positive deviations from the equilibrium angle more energetically favorable than negative deviations where the H_h approaches the ammonium group. As discussed in relation to nonrigid molecules and SDFs, this distortion smears the sampling and is manifested here as a leftward shift in the surface. However, this explanation implies a similar effect should be observed for the O_w surface, which is not the case. Alternatively, steric considerations would tend to favor positions slightly further from the ammonium group for anions that have hydrogen bonds with the hydroxyl group, particularly because there is no well-defined coordination between O_h and any other species in the system through the O_h lone pairs. As a related matter, nonlinearities in the cation−anion H-bonds near the hydroxyl group may also suggest that the O_n is acting as a bifurcated acceptor, forming an additional H-bond with another cation or water molecule. The more nonlinear the geometry, i.e., the more skewed the lobe, the weaker the hydrogen bond, and consequently the easier it is to form a secondary hydrogen bond. This possibility will be discussed in more detail in a later section. By the same argument, however, because the lobe does not stretch toward the ammonium group, it appears unlikely that a single O_n coordinates with both H_h and H_a hydrogens from the same cation.

https://doi.org/10.1021/acs.jpcb.3c05623
J. Phys. Chem. B 2024, 128, 824−840

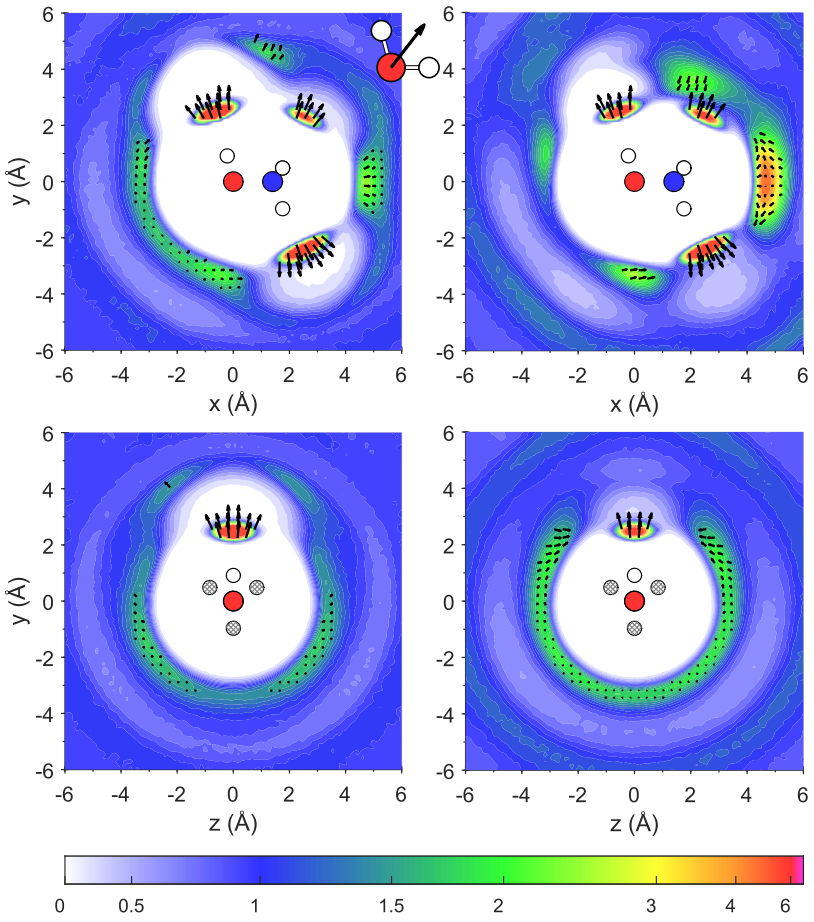

Figure 8. Water oxygen density plane projections in the hydroxylammonium cation vicinity in HAN at ion mole fractions of $\chi = 0.05$ (left) and $\chi = 0.77$ (right). The top row aligns the cation's σ mirror plane to the xy-plane, centered at the hydroxyl oxygen with the O−N bond on the $+x$-axis. The bottom row shows the yz-plane looking down at the O−N bond. Projections sample a width of 1 Å on either side of the respective plane. Atoms with a hatched fill in the bottom row lie outside of the sample region. Arrows indicate the average direction of the water dipole moment vector and are included in regions where $\hat{\rho}_{O_w} \geq 1.5$. Larger arrows indicate a higher likelihood of orientation.

In the ammonium region, the hydrogen bonds are generally linear, with neither the O_w nor the O_n surfaces exhibiting substantial nonlinearity at the contour level shown. This is the same behavior as seen in the CPMD simulations for MAN.[28] Interestingly, the larger primary alkylammonium nitrates EAN, PAN, and BAN were shown to contain mainly bent $N_h-H_h\cdots O_n$ hydrogen bonds.[23,60] The PILs with bent H-bonds have been characterized as more "liquid-like", whereas PILs with linear H-bonds are more "solid-like" with higher melting points.[23] This trend is therefore consistent with neat HAN and MAN, which have melting points of 44−48 and 105 °C, respectively.[5,6,61]

Interstitial Binding of Water. The shoulder in the O_w-O_n RDFs of Figure 4e at the two higher ion concentrations can be attributed to an increase in the level of water oxygen in the lobes above and below the nitrate in Figure 6b. The behavior of the water at the two concentration extremes can be visualized via a projection of the water oxygen density orthogonal to the nitrate plane, in essence summing a 2D slice of the SDF.[53] In Figure 7, the projection is constructed for $\chi = 0.05$ (left) and $\chi = 0.77$ (right) by placing one of the N−O bonds on the $+x$-axis, aligning the nitrate C_3 axis along the y-axis, and using a slice width of 1 Å on either side. The contours are normalized by $\hat{\rho}_{O_w}$, with blue regions indicating approximately bulk water density. It is clear that at low ion concentrations, only a weak hydration shell is formed, and water molecules may easily exchange with one another outside the immediate hydrogen-bonding region. At this concentration, the dark blue equatorial region at $x = 5-6$ Å in the left plot of the figure corresponds to the second RDF peak in Figure 4e at 4.59 Å (note that $b(N-O) = 1.27$ Å).

At the higher concentration, the geometry of the hydration shell is qualitatively similar to that at the lower concentration, but the structure is more defined. Also, it is important to note that the deep red region at $x = -3$ Å does not directly indicate an increase in hydrogen bonding. This is because the potential O_n acceptor atoms in this half of the molecule lie outside of the xy-plane. Nevertheless, their presence influences the sampling within this region, causing an apparent increase in the density of the O_w in the contour plot, even though the O_n atoms themselves are not a part of the sampled region.

The vector arrows in Figure 7 are centered at the water oxygen and depict the direction of the water dipole moment using the physicists' sign convention, where the vector points toward the positive part of the molecule.[62] A sample schematic in Figure 1 shows that the arrow points up and to the right from O_w, bisecting the water bond angle. Unsurprisingly, in the regions that contain the hydrogen-bonding O_w lobes that coordinate with the O_n lone pairs in Figure 6b, the water dipole vectors point toward the acceptor oxygen on average. Above and below these lobes, a brief transition region exists where the dipole quickly reverses direction. Note that, due to averaging in the z-

https://doi.org/10.1021/acs.jpcb.3c05623
J. Phys. Chem. B 2024, 128, 824−840

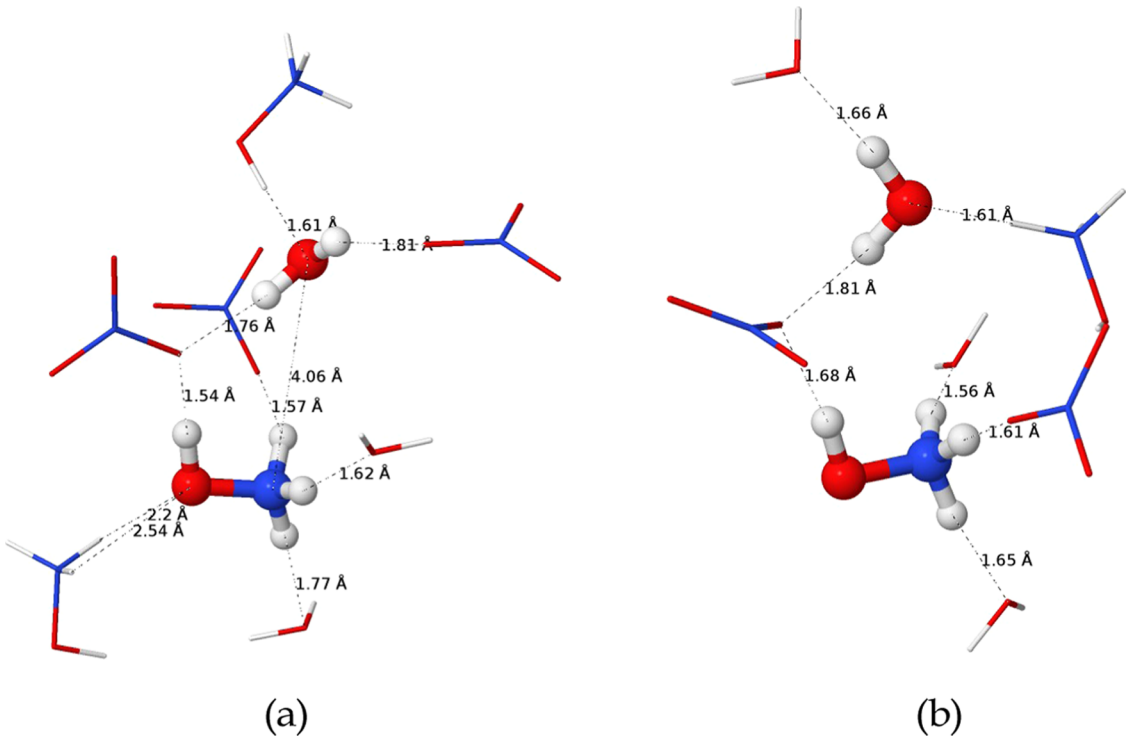

Figure 9. Snapshots of interstitial water coordination in HAN at ion mole fraction $\chi = 0.43$ in a bulk NVT simulation. Only the local H-bonding region is shown.

plane, an arrow pointing directly upward does not necessarily imply that the water dipole moment is most likely to align with the $+y$-axis. Rather, it suggests that a strong majority of dipole vectors form an angle $|\theta| < 90°$ with respect to the $+y$-axis, where θ is equally likely to be positive or negative. Indeed, further analysis of the water orientation in the axial lobe regions reveals an interesting pattern. The most probable orientation positions one H_w normal to the N_n-O_w vector, with the other H_w angled away from the anion center. Additional details about this geometry can be found in the Supporting Information (Figure S4).

The increased water density in the axial lobes at elevated ion concentrations is significant because no such lobes are observed for interionic species at similar values of $\hat{\rho}_{donor}$. The compact size of the water molecule enables the formation of a tight H-bonding network where a bridging water can situate in an otherwise unoccupied region above or below the anion. This configuration allows water to maximize its capacity as a hydrogen bond donor, but it does limit the ability of the O_w to form acceptor hydrogen bonds. The impact of this trade-off can be seen in the water coordination numbers presented in Table 3, as well as in the relative widths of the H_w and the O_w groups illustrated in Figure 5.

A similar analysis has been performed for water surrounding the cation at both concentration extremes. Figure 8 contains two plane projections each for the concentrations with mole fractions of $\chi = 0.05$ (left) and 0.77 (right). When computing the projections, the O_h, N_a, and H_h atoms were used to define the cation reference frame, which was centered at the hydroxyl oxygen with the O_h-N_a bond on the $+x$-axis. In this manner, the top row shows the hydroxylammonium's σ mirror plane, while the bottom row rotates the view by 90° to sample the yz-plane near the hydroxyl. The slice width of 1 Å on either side helps limit the smearing effect of the hydroxyl's low torsional barrier for the nonrigid molecule. Note that this clips the highest-density regions around the ammonium nitrogen, which correspond to the orange O_w lobes seen in the right half of Figure 6c, but the focus of this analysis is the secondary coordination of water around the cation.

Several significant changes in the water solvation structure occur near the cation as the ion concentration is increased. The first closely mirrors the enhanced axial O_w lobes seen above and below the nitrate in Figure 7. A similar axial lobe is apparent in the top row projections of Figure 8 at around $x = 4.5$ Å. The most important difference between the cation and anion axial lobes is that the nearest-neighbor counterions have opposite donor–acceptor character in these two cases. That is, for the anion in Figure 7, the nearest-neighbor hydroxylammonium counterion behaves exclusively as a hydrogen bond donor to the anion's O_n atoms, outcompeting the axial water and directing the water's dipole moment away from the anion. The opposite is true for the cation in Figure 8, where the nearest-neighbor nitrate counterion is solely an acceptor. Suppose the nearest-neighbor nitrate coordinates with the cation's ammonium group. Disregarding the O_n atom as a possible bifurcated acceptor, the nitrate still contains two additional acceptor sites. Consequently, the water molecules in the axial lobe region of Figure 8 can donate hydrogen bonds to this anion, leading to the different dipole vector directions observed in the figure. Note that at the lower concentration, there are insufficient H-bond acceptors in this region to divert the vectors, so the lobe in this region can be primarily ascribed to a weaker ion–dipole interaction instead of hydrogen bonding. The "axial lobe" water effect is amplified at higher concentrations for both ion species as additional water, which simultaneously functions as a donor *and* acceptor, is removed from the system.

The same argument can be applied to describe differences in the region around the hydroxyl. A weak and unstructured

https://doi.org/10.1021/acs.jpcb.3c05623
J. Phys. Chem. B 2024, 128, 824–840

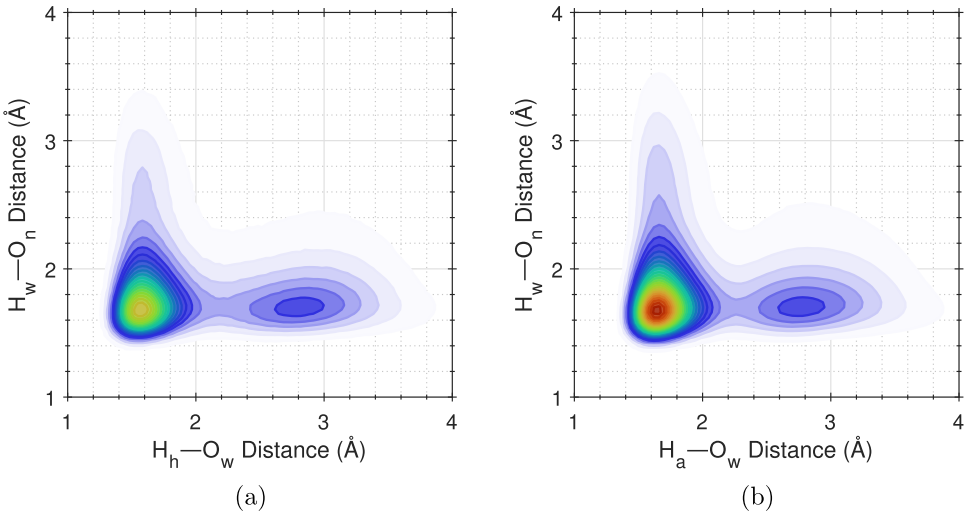

Figure 10. Combined distribution functions of nearest-neighbor intermolecular H−O distances for depicting water bridging with the hydroxylammonium cation in HAN at ion mole fraction $\chi = 0.43$.

hydration shell around the hydroxyl is refined as the anion population grows, creating preferred interstitial sites where the water molecules can act as H-bond donors. Three such sites can be identified near the hydroxyl in Figure 8. The first lies in the cation σ plane to the left of the O−N bond, and it tends to form a weak secondary hydrogen bond to the same O_n already coordinated with the cation's hydroxyl. The other two sites can be seen at the $\chi = 0.77$ ion mole fraction in the axial view (bottom) of Figure 8, connected as part of the same structure. An increased ion concentration results in a pronounced tendency for water to form secondary hydrogen bonds on either side of the σ plane, as shown by the strong directionality of the water dipole moment vectors flanking the acceptor site. The water has decent mobility in this region, however, and as it migrates around the cation O−N bond toward the rear of the hydroxyl below $y = 0$, the coordination shifts toward forming a secondary hydrogen bond with an acceptor (e.g., O_n) which is already coordinated with the ammonium group. This behavior cannot be deduced from just one of the plane projection views, as the directionality of the vectors is averaged away at the bottom of the axial view and the out-of-plane coordination at $|z| > 1$ Å is not sampled in the mirror plane view.

The presence of these secondary water hydrogen bonds formed with the hydroxyl-coordinated O_n contributes to the asymmetry in the salmon O_n lobe in the SDF (top left of Figure 6c). As the ion concentration increases, more water settles nearby, and the resulting secondary hydrogen bond weakens the primary hydrogen bond with the hydroxyl, leading toward a more nonlinear H-bond angle and stretching of the lobe. Since this asymmetry is not observed with hydroxyl-coordinated O_w at any concentration, it seems unlikely that O_w acts as a bifurcated acceptor when hydrogen-bonded to the cation's hydroxyl group.

Finally, the most notable difference between the concentration extremes is observed above the cation in the top row of Figure 8. At low concentrations, a small region of water around ($x = 1$ Å, $y = 4.5$ Å) can be attributed to the secondary hydration shell, where this water accepts a hydrogen bond from another hydroxyl-coordinated water. Indeed, the distance between these density maxima in Figure 8 is 2.74(12) Å, consistent with the measured O_w−O_w RDF maximum of 2.79 Å. Once again, note from the Sankey diagram (Figure 5) that over half of the hydroxyl H_a's hydrogen bond with water at $\chi = 0.05$, but this comparatively weak hydrogen bond is almost nonexistent at $\chi = 0.77$. Consequently, at high concentrations, water in the secondary shell can no longer act as an acceptor in this region, instead shifting closer to the ammonium group. This is a remarkably localized region with respect to the σ mirror plane so that it bisects the ammonium H_a−N_a−H_a angle. The directionality of the dipole vectors is somewhat misleading due to the averaging, but examination of snapshots from the trajectory shows that this water again forms secondary hydrogen bonds to a hydroxyl-coordinated O_n. Two such snapshots are shown in Figure 9 for HAN with $\chi = 0.43$, where the interstitial coordination is still pronounced. Corresponding density projections at this concentration are provided in Figures S5 and S6, which display qualitatively similar behavior to the $\chi = 0.77$ case.

To summarize, it is the development of the axial O_w lobes and refinement of the secondary hydration structure that drives many of the differences beyond the first peaks involving O_w in Figure 4. The water molecule's small size and dual roles as donor and acceptor are ideal for insertion into the complex H-bond network at interstitial sites. Because the nitrate oxygen can act as a bifurcated acceptor, as ion concentration increases, more water situates into these interstitial sites, leading to the negative excess molar volume observed at these concentrations. The enhanced hydrogen bonding consequently decreases the vapor pressure in aqueous HAN, enough so that the vapor pressures of these systems are lower than the vapor pressure of pure water at equivalent mole fractions.[63]

H-Bonding Network and Dynamics. HAN has been shown to be fully miscible with water at all concentrations up to the anhydrous salt.[9,10] The analysis of various interstitial binding sites around the ions from the previous section offers evidence for how water is accommodated in the structure of concentrated HAN. However, the plane projections only provide limited insight into the water molecules that are directly hydrogen-bonded to either ion species. This is because in these projections, the dipole vectors invariably point away from or toward the donor or acceptor atom of the ion, respectively. Alternatively, the role of water-bridging cations and anions can be investigated with combined distribution functions (CDFs) of hydrogen-acceptor distances. The $\chi = 0.43$ mole fraction is considered here due to the balanced representation of water and

https://doi.org/10.1021/acs.jpcb.3c05623
J. Phys. Chem. B 2024, 128, 824−840

ion species. In Figure 10, a single reference water molecule is used to plot cation−water distances on the *x*-axis and anion−water distances on the *y*-axis. For clarity, only the nearest-neighbor hydrogen and acceptor atoms in each molecule pair are considered in generating the plot. This prevents oversampling of H−O interactions at neighboring sites and limits misinterpreting of the primary mode of coordination. The light blue regions on the right of these plots therefore represent a water that is hydrogen-bonded to an anion but does not have a cation in its immediate vicinity. Because this region is inside the second peak in the H_a-O_w and H_h-O_w RDFs in Figure 3b, it is likely that the nearest-neighbor cation to this water molecule is forming a hydrogen bond with another oxygen on the same anion. In this case, the anion links the water and the cation rather than the water bridging the two opposing ion species. Complementary to the analysis from the RDFs and SDFs, the densely populated bridging regions highlight the tight structuring of these water molecules within the hydrogen-bonding network.

It is important to note that MD techniques based on classical force fields often lead to overestimation of the strength of ionic interactions in ILs, though the use of a polarizable force field is known to help mitigate this issue.[64−66] Simulation techniques that allow for reactivity and explicitly account for electronic effects, such as *ab initio* MD, may reveal an enhancement in the hydrogen or proton mobility. In that case, water-bridging structures such as those represented in Figure 10 could allow for Grotthuss-like proton transport. While such a mechanism may be possible—and indeed has been hypothesized in this system[17]—the primary mode of proton transfer in HAN is likely via direct transfer from the ammonium group to the nitrate. Thus, the number and stability of the $N_a-H_a\cdots O_n$ hydrogen bonds must be predominant factors in the reactivity of condensed-phase HAN. Figure 11 illustrates the concentration dependence for the distribution of such hydrogen bonds. A maximum of three hydrogen bonds are formed per ammonium group (no bifurcation is observed). Interestingly, over half of all cations have at least one $N_a-H_a\cdots O_n$ hydrogen bond across the range of mole fractions considered. At the lowest concentration, 60.3% of ammonium groups are hydrogen-bonded to a nitrate, whereas only 45.6% of the hydroxyl groups contain this hydrogen bond. As the concentration increases, more O_n sites become available, and the ammonium group is able to form additional strong hydrogen bonds with the nitrate. Once the ion mole fraction reaches 0.43, over 80% of the cations have either 2 or 3 hydrogen bonds capable of direct proton transfer to the nitrate. Taking into account the average per ammonium hydrogen (H_a) at $\chi = 0.43$, the results show that 73.2% of the H_a atoms participate in hydrogen bonds with a nitrate. This percentage rises further to 90.8% at $\chi = 0.77$, thus providing an abundance of routes for proton transfer in highly concentrated HAN.

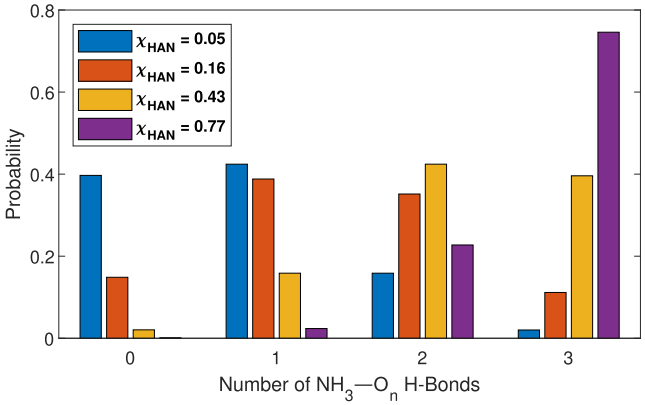

Figure 11. Distribution of $N_a-H_a\cdots O_n$ hydrogen bonds in HAN at different ion concentrations. The conditions for hydrogen bonding are specified in the text.

Finally, hydrogen bond dynamics is investigated in the context of lifetime estimates for each type. These hydrogen bond lifetimes are calculated using the reactive flux formalism as implemented in TRAVIS.[53,67] In this formalism, nonexponential relaxation of hydrogen bonds is treated with the kinetic equation

$$-\dot{c}(t) = k_d c(t) - k_f n(t) \tag{3}$$

where $c(t)$ is the probability that a hydrogen bond is intact at a time t (and was initially intact at time zero) and $n(t)$ is the probability that atoms which were initially hydrogen-bonded are now unbonded at time t but remain within a predefined vicinity of one another.[68] Consequently, k_d and k_f represent the rate constants for hydrogen bond decay (breaking) and reformation, respectively. From these definitions, the average hydrogen bond lifetime is determined from $\tau_{lt}^{HB} = 1/k_d$. This technique accounts for the different time scales associated with hydrogen bond dynamics and diffusion, reducing the noise associated with intermittent H-bond breaking and reformation.[68] However, because k_f only includes statistics for hydrogen bonds which are *known* to later reform, the reformation time $\tau_{ft}^{HB} = 1/k_f$ does not have any *explicit* physical meaning.[69,70]

In this analysis, the existence of a hydrogen bond is specified by two criteria: if the hydrogen-acceptor distance is less than the distance to the first minimum of the RDF, and if the donor-hydrogen/donor−acceptor angle is less than a predefined cutoff value. Often in the literature, a cutoff angle of 30° is used based on a suggestion by Luzar and Chandler.[68,71] While this is a suitable choice for the bulk water system they investigated, employing this rigid cutoff without regard to the underlying system would exclude many nonlinear H-bonds in protic ionic liquids, including EAN and PAN.[23] Gehrke and Kirchner[69] performed a sensitivity analysis for cutoff values on hydrogen bond lifetimes calculated with the reactive flux method and found that a 30° cutoff angle predicts substantially shorter lifetimes than their selected 60° cutoff, but angles larger than this up to 90° do not result in significantly different lifetimes. Because of the complex hydrogen-bonding environment in the HAN, this work uses the following detailed approach to select the cutoff angle. For each H-bond type in each simulation, a CDF is generated where the *x*-axis represents the hydrogen-acceptor distance and the *y*-axis shows the donor-hydrogen/donor−acceptor angle, plotted up to 90°—well beyond a physical representation of a hydrogen bond. Using the known distance for the first RDF minimum, a "rectangle" is constructed in the CDF that encapsulates the entirety of the dense region corresponding to hydrogen bonding, roughly up to any saddle point in the plot. The upper bound of this rectangle is then considered for the cutoff angle and subsequently checked against the SDFs to ensure that only the desired hydrogen-bonding interactions are sampled. All CDFs from this analysis are included in the Supporting Information (Figures S7−S12). This procedure leads to cutoff angles that include weak interactions for all H-bond types.

Values for τ_{lt}^{HB} and τ_{ft}^{HB} are reported for all H-bond types in Table 4. These results show that the shortest-lived hydrogen

https://doi.org/10.1021/acs.jpcb.3c05623
J. Phys. Chem. B 2024, 128, 824−840

Table 4. Hydrogen Bond Lifetimes (τ_{lt}^{HB}) and Reformation Times (τ_{ft}^{HB}) in HAN from the Reactive Flux Analysis (Values in ps)

	χ = 0.05		χ = 0.16		χ = 0.43		χ = 0.77	
hydrogen bond type	τ_{lt}^{HB}	τ_{ft}^{HB}	τ_{lt}^{HB}	τ_{ft}^{HB}	τ_{lt}^{HB}	τ_{ft}^{HB}	τ_{lt}^{HB}	τ_{ft}^{HB}
H_a-O_n	41.3	98.5	57.8	137.2	115.6	260.1	238.9	515.8
H_h-O_n	24.5	4.1	26.5	6.1	48.9	16.7	104.0	39.4
H_w-O_n	5.7	9.7	3.8	7.6	19.5	61.8	50.1	114.4
H_a-O_w	25.2	65.0	34.5	88.6	77.8	181.2	194.8	418.0
H_h-O_w	23.1	1.3	22.4	1.3	39.0	2.1	91.9	4.1
H_w-O_w	2.5	10.6	3.9	18.2	20.9	105.4	59.9	212.1

bonds are those where water acts as a donor, which is unsurprising as these are the longest and therefore weakest hydrogen bonds in the system. The longest-lived hydrogen bonds stem from the ammonium group with the doubly ionic $O_n\cdots H_a$ bond having the longest lifetime across all concentrations. It should be noted that the analysis was performed on a per-hydrogen basis; therefore, these results do not explicitly consider the collective lifetime of *all* ammonium group hydrogen bonds. That these ammonium H-bonds have longer lifetimes than the stronger hydroxyl H-bonds seems counterintuitive, but it can be explained by the extremely low torsion barrier about the cation's N−O bond—the hydroxyl can readily rotate away from the acceptor while leaving the ammonium H-bonds intact, but an analogous rotation of the ammonium group would likely require simultaneously breaking multiple H-bonds. Increasing the ion concentration slows the dynamics and leads to larger lifetimes for almost all H-bond types, though the effect is most pronounced once the mole fraction reaches χ = 0.43. It would be interesting to perform additional simulations at intermediate mole fractions between the second and third values in order to determine at what concentration the lifetimes begin to rapidly increase.

Protic ionic liquids in concentrated aqueous solution typically exhibit faster dynamics (diffusivity, viscosity) as water content increases,[25,72,73] and this behavior has previously been observed experimentally in HAN.[74] Disruption in the H-bond network is known to affect viscosity in PIL mixtures.[21] This is consistent with the shift in structure discussed in the previous section, as water is readily accommodated at interstitial sites in concentrated HAN, but it becomes structure-breaking upon further dilution. Weakening of the H-bond network is apparent in the reduced lifetimes at low ion mole fractions. From an electrostatic perspective, ion pair dissociation is correlated with the screening of strong Coulomb interactions by the introduction of the polar solvent, which in turn increases the fluidity of the liquid mixture.

CONCLUSIONS

The bulk liquid structure of aqueous HAN was investigated over a range of concentrations via polarizable MD simulations conducted at 298 K. A negative excess molar volume was predicted for all concentrations considered. HAN is unique in its composition compared to other ammonium-based nitrates—and indeed, most other protic ionic liquids—because its relatively small cation contains strong hydrogen bond donors in both of its functional groups. Simulations confirmed the existence of a dense, three-dimensional hydrogen-bonding network characterized by short and strong doubly ionic H-bonds. The $O_h-H_h\cdots O_n$ bond between the cation's hydroxyl group and the anion was shown to be the strongest hydrogen bond in the system, while simultaneously displaying the weakest directionality due to the facile rotation of the hydroxyl about the cation N−O bond and its ability to form bifurcated hydrogen bonds.

The addition of water does not destroy this network in concentrated HAN solutions. Instead, water was found to be incorporated into the hydrogen-bonding network, occupying interstitial sites around the ions. This provides a rationale for the notably high miscibility of HAN with water as well as the negative excess molar volume observed. Qualitatively, these results are consistent with previous conclusions that concentrated HAN behaves as a molten salt.[63] Thus, the frequent referral to aqueous HAN as an "ionic liquid" in engineering applications is not entirely unfounded at high concentrations. Further study of ion and water aggregate sizes at different concentrations may provide additional insight into this behavior. Figures S13 and S14 in the Supporting Information suggest that small ion aggregates exist at χ = 0.05, but aggregation of water molecules is rare at χ = 0.77.

A transition region in the behavior of aqueous HAN was identified between the two intermediate concentrations simulated with χ = 0.16 and 0.43. Both the structure and dynamics of the hydrogen-bonding network shift in this region as increasing ion concentration reduces the hydration of the anion and doubly ionic hydrogen bonds start to dominate. This leads to enhanced ion aggregation and substantially longer hydrogen bond lifetimes, as strong electrostatic interactions are less effectively screened by the polar solvent.

HAN's demonstrated potential as a spacecraft propellant underscores the importance of proton transfer in the initial steps of decomposition. Liquid structure is an essential component alongside energetics in understanding proton transfer in the condensed phase. Assuming that direct proton transfer from the ammonium group to the nitrate is the primary process governing reactivity, coordination via $N_a-H_a\cdots O_n$ hydrogen bonding is a necessary precursor event. In dilute solutions, the competitive hydrogen-bonding environment with the nitrate favors the hydroxyl, relegating most ammonium H_a atoms to a hydrogen bond with water. However, at an ion mole fraction of χ = 0.43, a suitable concentration for propulsion applications, nearly 75% of ammonium H_a atoms form a hydrogen bond with a nitrate oxygen. Thus, from a purely structural argument, increasing the concentration of HAN will promote proton transfer and decomposition.

ASSOCIATED CONTENT

Supporting Information

The Supporting Information is available free of charge at https://pubs.acs.org/doi/10.1021/acs.jpcb.3c05623.

Additional figures including density plots for NPT simulations, combined distribution functions of water molecule orientations, and combined distribution functions used to define hydrogen bonds in the text (PDF)

https://doi.org/10.1021/acs.jpcb.3c05623
J. Phys. Chem. B 2024, 128, 824−840

AUTHOR INFORMATION

Corresponding Author

Ghanshyam L. Vaghjiani − *Aerospace Systems Directorate, Air Force Research Laboratory, AFRL/RQRS, Edwards Air Force Base, California 93524, United States;* orcid.org/0000-0001-7473-7388; Email: ghanshyam.vaghjiani@spaceforce.mil

Authors

Daniel D. Depew − *Department of Astronautical Engineering, University of Southern California, Los Angeles, California 90089, United States*

Shehan M. Parmar − *Department of Chemistry and Biochemistry, Georgia Institute of Technology, Atlanta, Georgia 30332, United States*

Joseph J. Wang − *Department of Astronautical Engineering, University of Southern California, Los Angeles, California 90089, United States*

Complete contact information is available at: https://pubs.acs.org/10.1021/acs.jpcb.3c05623

Notes

The authors declare no competing financial interest.

ACKNOWLEDGMENTS

This work was supported by an Educational Partnership Agreement with the Air Force Research Laboratory under grant no. 19-EPA-RQ-07. This work was supported in part by high-performance computer time and resources from the DoD High-Performance Computing Modernization Program. The authors acknowledge the Center for Advanced Research Computing (CARC) at the University of Southern California for providing computing resources that have contributed to the research results reported within this publication. URL: https://carc.usc.edu. The first author is grateful to Kylar Flynn for assistance in the preparation of several graphics in the main text.

REFERENCES

(1) Gohardani, A. S.; Stanojev, J.; Demairé, A.; Anflo, K.; Persson, M.; Wingborg, N.; Nilsson, C. Green Space Propulsion: Opportunities and Prospects. *Prog. Aerosp. Sci.* **2014**, *71*, 128−149.

(2) Amrousse, R.; Katsumi, T.; Azuma, N.; Hori, K. Hydroxylammonium Nitrate (HAN)- Based Green Propellant as Alternative Energy Resource for Potential Hydrazine Substitution: From Lab Scale to Pilot Plant Scale-Up. *Combust. Flame* **2017**, *176*, 334−348.

(3) Jankovsky, R. S. In *HAN-based Monopropellant Assessment for Spacecraft*, 32nd Joint Propulsion Conference and Exhibit, 1996.

(4) Hawkins, T. W.; Brand, A. J.; McKay, M. B.; Tinnirello, M. In *Reduced Toxicity, High Performance Monopropellant at the U.S. Air Force Research Laboratory*, Making Safety Matter, Proceedings of the Fourth IAASS Conference. Huntsville, Alabama, 2010.

(5) Klein, N. *The Molecular Structure of the HAN-Based Liquid Propellants*; Technical Report BRL-TR-3139; US Army Ballistic Research Laboratory: Aberdeen Proving Ground, MD, 1990.

(6) Freudenmann, D.; Ciezki, H. K. ADN and HAN-Based Monopropellants − A Minireview on Compatibility and Chemical Stability in Aqueous Media. *Propellants, Explos., Pyrotech.* **2019**, *44*, 1084−1089.

(7) Greaves, T. L.; Drummond, C. J. Protic Ionic Liquids: Properties and Applications. *Chem. Rev.* **2008**, *108*, 206−237.

(8) Lei, Z.; Chen, B.; Koo, Y. M.; Macfarlane, D. R. Introduction: Ionic Liquids. *Chem. Rev.* **2017**, *117*, 6633−6635.

(9) Klein, N. *Liquid Propellants for Use in Guns - A Review*; Technical Report BRL-TR-2641; US Army Ballistic Research Laboratory: Aberdeen Proving Ground, MD, 1985.

(10) Vosen, S. R. Concentration and Pressure Effects on the Decomposition Rate of Aqueous Hydroxylammonium Nitrate Solutions. *Combust. Sci. Technol.* **1989**, *68*, 85−99.

(11) Chambreau, S. D.; Popolan-Vaida, D. M.; Vaghjiani, G. L.; Leone, S. R. Catalytic Decomposition of Hydroxylammonium Nitrate Ionic Liquid: Enhancement of NO Formation. *J. Phys. Chem. Lett.* **2017**, *8*, 2126−2130.

(12) Oxley, J. C.; Brower, K. R. Thermal Decomposition Of Hydroxylamine Nitrate. *Propulsion* **1988**, 63.

(13) Pembridge, J. R.; Stedman, G. Kinetics, Mechanism, and Stoicheiometry of the Oxidation of Hydroxylamine by Nitric Acid. *J. Chem. Soc., Dalton Trans.* **1979**, 1657−1663.

(14) Cronin, J. T.; Brill, T. B. Thermal Decomposition of Energetic Materials. 8. Evidence of an Oscillating Process during the High-Rate Thermolysis of Hydroxylammonium Nitrate, and Comments on the Interionic Interactions. *J. Phys. Chem. A* **1986**, *90*, 178−181.

(15) Rafeev, V. A.; Rubtsov, Y. I. Kinetics and Mechanism of Thermal Decomposition of Hydroxylammonium Nitrate. *Russ. Chem. Bull.* **1993**, *42*, 1811−1815.

(16) Schoppelrei, J. W.; Brill, T. B. Spectroscopy of Hydrothermal Reactions. 7. Kinetics of Aqueous [NH3OH]NO3 at 463−523 K and 27.5 MPa by Infrared Spectroscopy. *J. Phys. Chem. A* **1997**, *101*, 8593−8596.

(17) Lee, H. S.; Litzinger, T. A. Chemical Kinetic Study of HAN Decomposition. *Combust. Flame* **2003**, *135*, 151−169.

(18) Ashcraft, R. W.; Raman, S.; Green, W. H. Ab Initio Aqueous Thermochemistry: Application to the Oxidation of Hydroxylamine in Nitric Acid Solution. *J. Phys. Chem. B* **2007**, *111*, 11968−11983.

(19) Esparza, A. A.; Ferguson, R. E.; Choudhuri, A.; Love, N. D.; Shafirovich, E. Thermoanalytical Studies on the Thermal and Catalytic Decomposition of Aqueous Hydroxy- lammonium Nitrate Solution. *Combust. Flame* **2018**, *193*, 417−423.

(20) Zhang, K.; Thynell, S. T. Thermal Decomposition Mechanism of Aqueous Hydroxylammonium Nitrate (HAN): Molecular Simulation and Kinetic Modeling. *J. Phys. Chem. A* **2018**, *122*, 8086−8100.

(21) Smith, J. A.; Webber, G. B.; Warr, G. G.; Atkin, R. Rheology of Protic Ionic Liquids and Their Mixtures. *J. Phys. Chem. B* **2013**, *117*, 13930−13935.

(22) Chatel, G.; Pereira, J. F.; Debbeti, V.; Wang, H.; Rogers, R. D. Mixing Ionic Liquids- "simple Mixtures" or "Double Salts"? *Green Chem.* **2014**, *16*, 2051−2083.

(23) Hayes, R.; Imberti, S.; Warr, G. G.; Atkin, R. The Nature of Hydrogen Bonding in Protic Ionic Liquids. *Angew. Chem., Int. Ed.* **2013**, *52*, 4623−4627.

(24) Hayes, R.; Warr, G. G.; Atkin, R. Structure and Nanostructure in Ionic Liquids. *Chem. Rev.* **2015**, *115*, 6357−6426.

(25) Greaves, T. L.; Drummond, C. J. Protic Ionic Liquids: Evolving Structure-Property Relationships and Expanding Applications. *Chem. Rev.* **2015**, *115*, 11379−11448.

(26) Fumino, K.; Wulf, A.; Ludwig, R. Hydrogen Bonding in Protic Ionic Liquids: Reminiscent of Water. *Angew. Chem., Int. Ed.* **2009**, *48*, 3184−3186.

(27) Greaves, T. L.; Kennedy, D. F.; Mudie, S. T.; Drummond, C. J. Diversity Observed in the Nanostructure of Protic Ionic Liquids. *J. Phys. Chem. B* **2010**, *114*, 10022−10031.

(28) Zahn, S.; Thar, J.; Kirchner, B. Structure and Dynamics of the Protic Ionic Liquid Monomethylammonium Nitrate ([CH3NH3][NO3]) from Ab Initio Molecular Dynamics Simulations. *J. Chem. Phys.* **2010**, *132*, No. 124506.

(29) Zahn, S.; Wendler, K.; Delle Site, L.; Kirchner, B. Depolarization of Water in Protic Ionic Liquids. *Phys. Chem. Chem. Phys.* **2011**, *13*, 15083−15093.

(30) Greaves, T. L.; Kennedy, D. F.; Weerawardena, A.; Tse, N. M.; Kirby, N.; Drummond, C. J. Nanostructured Protic Ionic Liquids Retain Nanoscale Features in Aque ous Solution While Precursor Brønsted Acids and Bases Exhibit Different Behavior. *J. Phys. Chem. B* **2011**, *115*, 2055−2066.

(31) Hayes, R.; Imberti, S.; Warr, G. G.; Atkin, R. Amphiphilicity Determines Nanostructure in Protic Ionic Liquids. *Phys. Chem. Chem. Phys.* **2011**, *13*, 3237−3247.
(32) Hayes, R.; Imberti, S.; Warr, G. G.; Atkin, R. Pronounced Sponge-like Nanostructure in Propylammonium Nitrate. *Phys. Chem. Chem. Phys.* **2011**, *13*, 13544−13551.
(33) Porcedda, S.; Marongiu, B.; Schirru, M.; Falconieri, D.; Piras, A. Excess Enthalpy and Excess Volume for Binary Systems of Two Ionic Liquids + Water. *J. Therm. Anal. Calorim.* **2011**, *103*, 29−33.
(34) Canongia Lopes, J. N.; Esperança, J. M.; De Ferro, A. M.; Pereiro, A. B.; Plechkova, N. V.; Rebelo, L. P.; Seddon, K. R.; Vázquez-Fernández, I. Protonic Ammonium Nitrate Ionic Liquids and Their Mixtures: Insights into Their Thermophysical Behavior. *J. Phys. Chem. B* **2016**, *120*, 2397−2406.
(35) Campetella, M.; Macchiagodena, M.; Gontrani, L.; Kirchner, B. Effect of Alkyl Chain Length in Protic Ionic Liquids: An AIMD Perspective. *Mol. Phys.* **2017**, *115*, 1582−1589.
(36) Hunt, P. A.; Ashworth, C. R.; Matthews, R. P. Hydrogen Bonding in Ionic Liquids. *Chem. Soc. Rev.* **2015**, *44*, 1257−1288.
(37) Kempter, V.; Kirchner, B. The Role of Hydrogen Atoms in Interactions Involving Imidazolium-Based Ionic Liquids. *J. Mol. Struct.* **2010**, *972*, 22−34.
(38) Rheingold, A. L.; Cronin, J. T.; Brill, T. B.; Ross, F. K. Structure of Hydroxylammonium Nitrate (HAN) and the Deuterium Homolog. *Acta Crystallogr., Sect. C: Cryst. Struct. Commun.* **1987**, *43*, 402−404.
(39) Klein, N.; Wong, K. N. *An Infra-Red Investigation of HAN (Hydroxylammonium Nitrate)-Based Liquid Propellants*; Technical Report BRL-TR-2850; US Army Ballistic Research Laboratory: Aberdeen Proving Ground, MD, 1987.
(40) Borodin, O. Polarizable Force Field Development and Molecular Dynamics Simulations of Ionic Liquids. *J. Phys. Chem. B* **2009**, *113*, 11463−11478.
(41) Bedrov, D.; Borodin, O. Thermodynamic, Dynamic, and Structural Properties of Ionic Liquids Comprised of 1-Butyl-3-Methylimidazolium Cation and Nitrate, Azide, or Dicyanamide Anions. *J. Phys. Chem. B* **2010**, *114*, 12802−12810.
(42) Lamoureux, G.; MacKerell, A. D.; Roux, B. A Simple Polarizable Model of Water Based on Classical Drude Oscillators. *J. Chem. Phys.* **2003**, *119*, 5185.
(43) Thole, B. T. Molecular Polarizabilities Calculated with a Modified Dipole Interaction. *Chem. Phys.* **1981**, *59*, 341−350.
(44) Palmer, B. J. Direct Application of Shake to the Velocity Verlet Algorithm. *J. Comput. Phys.* **1993**, *104*, 470−472.
(45) Martyna, G. J.; Tuckerman, M. E.; Tobias, D. J.; Klein, M. L. Explicit Reversible Integrators for Extended Systems Dynamics. *Mol. Phys.* **1996**, *87*, 1117−1157.
(46) Sasse, R. A.; Davies, M. A.; Fifer, R. A.; Decker, M. M.; Kotlar, A. J. *Density of Hydroxylammonium Nitrate Solutions*; Technical Report BRL-MR-3720; US Army Ballistic Research Laboratory: Aberdeen Proving Ground, MD, 1988.
(47) Bahadur, I.; Letcher, T. M.; Singh, S.; Redhi, G. G.; Venkatesu, P.; Ramjugernath, D. Excess Molar Volumes of Binary Mixtures (an Ionic Liquid + Water): A Review. *J. Chem. Thermodyn.* **2015**, *82*, 34−46.
(48) Vizoso, S.; Rode, B. M. The Structure of Hydroxylamine — Water Mixtures Results of Monte Carlo Simulations. *Z. Naturforsch., A: Phys. Sci.* **1995**, *50*, 263−273.
(49) Gilli, G.; Gilli, P. *The Nature of the Hydrogen Bond*; Oxford University Press: New York, 2009.
(50) McDaniel, J. G.; Son, C. Y. Ion Correlation and Collective Dynamics in BMIM/BF4- Based Organic Electrolytes: From Dilute Solutions to the Ionic Liquid Limit. *J. Phys. Chem. B* **2018**, *122*, 7154−7169.
(51) Cammarata, L.; Kazarian, S. G.; Salter, P. A.; Welton, T. Molecular States of Water in Room Temperature Ionic Liquids. *Phys. Chem. Chem. Phys.* **2001**, *3*, 5192−5200.
(52) Brehm, M.; Kirchner, B. TRAVIS - A Free Analyzer and Visualizer for Monte Carlo and Molecular Dynamics Trajectories. *J. Chem. Inf. Model.* **2011**, *51*, 2007−2023.
(53) Brehm, M.; Thomas, M.; Gehrke, S.; Kirchner, B. TRAVIS—A Free Analyzer for Trajectories from Molecular Simulation. *J. Chem. Phys.* **2020**, *152*, No. 164105.
(54) Kusalik, P. G.; Svishchev, I. M. The Spatial Structure in Liquid Water. *Science* **1994**, *265*, 1219−1221.
(55) Mantz, Y. A.; Chen, B.; Martyna, G. J. Structural Correlations and Motifs in Liquid Water at Selected Temperatures: Ab Initio and Empirical Model Predictions. *J. Phys. Chem. B* **2006**, *110*, 3540−3554.
(56) Tongraar, A.; Tangkawanwanit, P.; Rode, B. M. A Combined QM/MM Molecular Dynamics Simulations Study of Nitrate Anion (NO3-) in Aqueous Solution. *J. Phys. Chem. A* **2006**, *110*, 12918−12926.
(57) Yadav, S.; Choudhary, A.; Chandra, A. A First-Principles Molecular Dynamics Study of the Solvation Shell Structure, Vibrational Spectra, Polarity, and Dynamics around a Nitrate Ion in Aqueous Solution. *J. Phys. Chem. B* **2017**, *121*, 9032−9044.
(58) Docampo-Álvarez, B.; Gómez-González, V.; Méndez-Morales, T.; Carrete, J.; Rodríguez, J. R.; Cabeza, Ó.; Gallego, L. J.; Varela, L. M. Mixtures of Protic Ionic Liquids and Molecular Cosolvents: A Molecular Dynamics Simulation. *J. Chem. Phys.* **2014**, *140*, No. 214502.
(59) Depew, D. D.; Wang, J. J.; Parmar, S. M.; Chambreau, S. D.; Bedrov, D.; van Duin, A.; Vaghjiani, G. L. In *Thermal Decomposition of Hydroxylammonium Nitrate: Reaxff Training Set Development for Molecular Dynamics Simulations*, AIAA Propulsion and Energy Forum and Exposition 2019, **2019**.
(60) Song, X.; Hamano, H.; Minofar, B.; Kanzaki, R.; Fujii, K.; Kameda, Y.; Kohara, S.; Watanabe, M.; Ishiguro, S.-i.; Umebayashi, Y. Structural Heterogeneity and Unique Distorted Hydrogen Bonding in Primary Ammonium Nitrate Ionic Liquids Studied by High-Energy X-ray Diffraction Experiments and MD Simulations. *J. Phys. Chem. B* **2012**, *116*, 2801−2813.
(61) Belieres, J. P.; Angell, C. A. Protic Ionic Liquids: Preparation, Characterization, and Proton Free Energy Level Representation. *J. Phys. Chem. B* **2007**, *111*, 4926−4937.
(62) Hovick, J. W.; Poler, J. C. Misconceptions in Sign Conventions: Flipping the Electric Dipole Moment. *J. Chem. Educ.* **2005**, *82*, 889.
(63) Decker, M. M.; Klein, N.; Freedman, E.; Leveritt, C. S.; Wojciechowski, J. Q. *HAN- Based Liquid Gun Propellants: Physical Properties*; Technical Report BRL-TR-2864; US Army Ballistic Research Laboratory: Aberdeen Proving Ground, MD, 1987.
(64) Thøgersen, J.; Réhault, J.; Odelius, M.; Ogden, T.; Jena, N. K.; Jensen, S. J.; Keiding, S. R.; Helbing, J. Hydration Dynamics of Aqueous Nitrate. *J. Phys. Chem. B* **2013**, *117*, 3376−3388.
(65) Yan, T.; Wang, Y.; Knox, C. On the Structure of Ionic Liquids: Comparisons between Electronically Polarizable and Nonpolarizable Models I. *J. Phys. Chem. B* **2010**, *114*, 6905−6921.
(66) Bedrov, D.; Piquemal, J. P.; Borodin, O.; MacKerell, A. D.; Roux, B.; Schröder, C. Molecular Dynamics Simulations of Ionic Liquids and Electrolytes Using Polarizable Force Fields. *Chem. Rev.* **2019**, *119*, 7940−7995.
(67) Gehrke, S.; von Domaros, M.; Clark, R.; Holl′oczki, O.; Brehm, M.; Welton, T.; Luzar, A.; Kirchner, B. Structure and Lifetimes in Ionic Liquids and Their Mixtures. *Faraday Discuss.* **2018**, *206*, 219−245.
(68) Luzar, A.; Chandler, D. Hydrogen-Bond Kinetics in Liquid Water. *Nature* **1996**, *379*, 55−57.
(69) Gehrke, S.; Kirchner, B. Robustness of the Hydrogen Bond and Ion Pair Dynamics in Ionic Liquids to Different Parameters from the Reactive Flux Method. *J. Chem. Eng. Data* **2020**, *65*, 1146−1158.
(70) Luzar, A. Resolving the Hydrogen Bond Dynamics Conundrum. *J. Chem. Phys.* **2000**, *113*, 10663.
(71) Luzar, A.; Chandler, D. Effect of Environment on Hydrogen Bond Dynamics in Liquid Water. *Phys. Rev. Lett.* **1996**, *76*, 928−931.
(72) Perron, G.; Hardy, A.; Justice, J. C.; Desnoyers, J. E. Model System for Concentrated Electrolyte Solutions: Thermodynamic and Transport Properties of Ethylammonium Nitrate in Acetonitrile and in Water. *J. Solution Chem.* **1993**, *22*, 1159−1178.
(73) Zarrougui, R.; Dhahbi, M.; Lemordant, D. Transport and Thermodynamic Properties of Ethylammonium Nitrate-Water Binary

Mixtures: Effect of Temperature and Composition. *J. Solution Chem.* **2015**, *44*, 686−702.
(74) Vanderhoff, J. A.; Bunte, S. W.; Donmoyer, P. M. *Electrical Conductance of Liquid Propellants: Theory and Results*; Technical Report BRL-TR-2741; US Army Ballistic Research Laboratory: Aberdeen Proving Ground, MD, 1986.

https://doi.org/10.1021/acs.jpcb.3c05623
J. Phys. Chem. B 2024, 128, 824−840